1-1-2011

# Critical Phenomena in Gravitational Collapses of Neutron Star Systems

Kejian Jin
*Washington University in St. Louis*

WASHINGTON UNIVERSITY

Department of Physics

Dissertation Examination Committee:
Wai-Mo Suen, Chair
Quo-Shin Chi
Ramanath Cowsik
Henric Krawczynski
Xiang Tang
Clifford M. Will

# CRITICAL PHENOMENA IN GRAVITATIONAL COLLAPSES OF NEUTRON STAR SYSTEMS

by

Kejian Jin

A dissertation presented to the
Graduate School of Arts and Sciences
of Washington University in
partial fulfillment of the
requirements for the degree
of Doctor of Philosophy

August 2011

Saint Louis, Missouri

# Abstract

We study critical phenomena in gravitational collapses of stellar objects based on numerical solutions of the Einstein equations.

We discovered that stellar objects with large kinetic energy described by an equation of state (EOS) commonly used in describing neutron star matter may undergo critical collapses. To the best of our knowledge, this is the first study showing that critical collapses can occur without postulating an exotic EOS.

We further showed that the critical collapses can occur due to an adiabatic change of the EOS, without fine tuning of the initial conditions. This opens the possibility that a neutron-star-like compact object with substantial kinetic energy, e.g. one newly formed in a supernova or in a binary coalescence, may undergo a critical collapse in processes which change the EOS, such as cooling.

We investigated the properties of the critical solutions of this system. We found, surprisingly, that there are branches of critical solutions, and a complicated phase diagram not been seen in other critical collapse studies.

The numerical simulations were carried out based on the full set of the Einstein equations coupled to the general relativistic hydrodynamic equations. The code we

constructed, GRAstro-2D, assumed axisymmetry to achieve high enough resolution needed for the study.

# Acknowledgements

I thank Professor Wai-Mo Suen for guidance and Drs. Jian Tao, Malcolm Tobias, Mew Bing Wan, Randy Wolfmeyer and Hui-Min Zhang for collaboration and discussions throughout the years of the research leading to this thesis.

The computer code GR-Astro-2D used in this research is based on the GR-Astro code which were written and supported by Mark Miller, Ed Evans, Philip Gressman, Sai Iyer, Hui-Min Zhang and others. The parallel computation layer of this code is based on the Cactus Toolkit developed by Tom Goodal and the Cactus support group.

The research is partially supported by NASA NCCS 5-153, NSF Phy 99-79985, NSF NRAC MCA93S025, DFG SFB382 and the McDonnell Center for Space Science at the Washington University.

# Contents

# Chapter 1

# Introduction

An isolated matter distribution in general relativity will evolve to one of three states: 1. a black hole (or a naked singularity), 2. a star (a non-singular self-gravitating object), and 3. the empty space (dispersal to infinity). In forming state 1 or 2, part of the distribution may also disperse to infinity. Critical phenomena were first found by Choptuik [1] at the dividing surface between 1 and 3; this is the so-called type II critical collapse (with a black hole mass that could be arbitrarily small); which most existing studies focus on (for review, see [2, 3, 4]). For a wide range of physical systems, including massless and massive scalar fields (real or complex) with different curvature couplings, "stiff" fluid ($P = K\rho$) for a range of constant $K$, pure gravitational radiation spacetimes, 2-D sigma models, $SU(2)$ Yang Mills field, SU(2) Skyrme field, SO(3) Mexican hat model, in alternative gravitational theories (Brans-Dicke, tensor-multi-scalar, or general relativity with a cosmological constant), and in 2+1 dimension or higher than 4 dimensions, critical collapse phenomena have

been found at the boundary between 1 and 3 [3]. There are also a few investigations at the boundary between 1 and 2 (the type I critical collapse, with a mass gap) for massive scalar field, SU(2) fields and collisionless matter [5, 6, 7].

The key property of critical collapse is the existence of an intermediate attractor (IA) at the threshold of black hole formation. When the initial matter distribution has a parameter $p$ close enough to its critical value $p_*$, the system will evolve towards the IA (the critical solution) for some length in time depending on the value of $p-p_*$, until the unstable mode of the IA kicks in to drive it to collapse (for $p > p_*$, super-critical) or disperse (for $p < p_*$, sub-critical), as shown by the trajectories in Fig. 1.1. In this figure, the IA, which is the critical solution, is static. In Fig. 1.2 the IA is a limit cycle, representing a periodic critical solution. Here we assume the IA has only one unstable mode, as is in all confirmed cases of critical collapse up to now. The two figures are reproduced from Gundlach [3]. There is universality in the sense that the parameter $p$ can be any parameter of the initial distribution that connects the black hole and the dispersed solution, e.g., $p$ can be the density, a size parameter of the system or the imploding velocity. Independent of how one chooses $p$, and hence for a range of different initial setups in many dimensions in phase space (a range of co-dimension one), the eventual collapses to black hole (or dispersal to infinity) behave practically the same, as they are governed by the same unstable mode of the IA. The property of this unstable mode depends only on the physics model, e.g., the EOS, but not on the initial data. Associated with this unstable mode there are other interesting properties of the critical phenomena including scaling of the mass of the

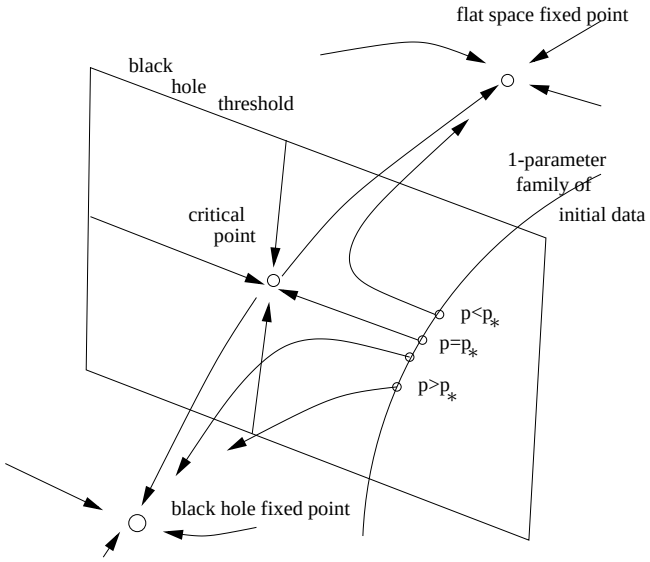


Figure 1.1: The phase space diagram for the black hole threshold in the presence of a critical point. The arrows show time evolutions of the spacetimes. The line without an arrow is not a time evolution, but a 1-parameter family of initial data that crosses the black hole threshold at $p = p_*$.

black hole formed (for type II critical collapses) and self similarity of the spacetime. The study of the critical collapse phenomena has led to new understanding of the properties of the solution space near the dividing lines of the 3 "phases".

Can critical collapses actually occur in nature? This is the main motivation of our investigation. This question has not been previously investigated for good reasons: All configurations found up to now that showed critical behavior are *not* expected to be common in nature. The problem is not so much that the matter sources are often exotic, e.g., stiff fluid, but that the initial configuration has to be fine tuned, with $(p - p_*)/p_*$ many orders of magnitude less than 1. That is, only those configurations

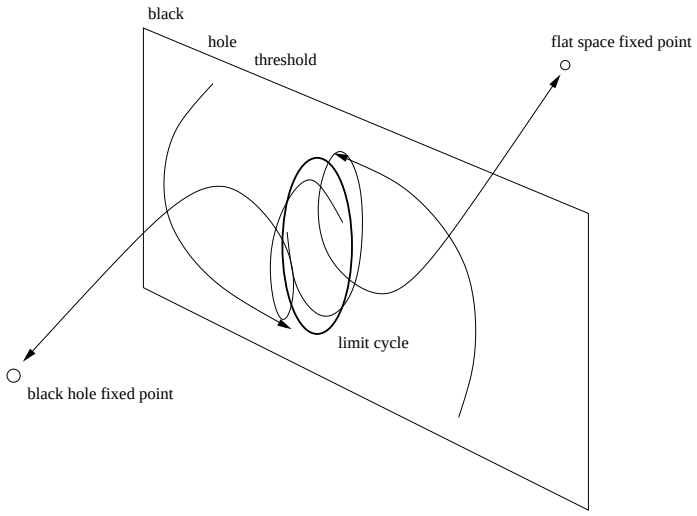


Figure 1.2: The phase space diagram in the case that the IA is a limit cycle. The plane represents the critical surface. The circle (fat unbroken line) is the limit cycle representing the critical solution. Shown also are two trajectories near the critical surfaces and therefore attracted to the limit cycle, and two trajectories out of the critical surface as the unstable mode of the IA finally sets in.

with, say, the central density $\rho$ (for $p$ chosen to be $\rho$) tuned very close to the critical value $\rho_*$ can get funneled to the IA and have the critical unstable mode dominate its collapse or dispersal. Unless one can find an astrophysics process that preferentially drives the density to the particular value $\rho_*$, one might not expect to observe critical collapse phenomena in nature.

We investigate this question by following a particular physical process in forming a compact object which could be at the boundary surface between evolving to a black hole or a one-singular stellar object. We choose to look at the end point of a binary neutron star (NS) coalescence. It is well known that such coalescence can lead to either a black hole or a hypermassive neutron star [8]. We follow the coalescence process through a numerical evolution of the Einstein equations coupled to the general

relativistic hydrodynamic equations [9]. The system of partial differential equations is arguably the most complicated set of differential equations for which a numerical solution is ever attempted. To achieve the resolution required for the study of the critical collapse, we restrict the study to that of the axisymmetric situation, which amounts to approximating the final plunge of the binary coalescence as a head on collision.

We construct the GRAstro-2D code, which takes advantage of the axisymmetry to provide high resolution in solving the coupled Einstein - general relativistic hydrodynamic equations. The reformulation of the Einstein equations that enables a numerical solution of the equation is given in Chapter 2. The construction and the validation of the GRAstro-2D code is given in Chapter 3.

The main results obtained are given in Chapter 4. Sec. 4.1 specifies the physical system in full detail. Sec. 4.3 gives evidence for the existence of the type I critical phenomena in head-on collision of neutron stars.

We found that in the super-critical regime, the merged object collapses promptly to form a black hole, even though its mass could be *less* than the maximum stable mass of one single NS in equilibrium with the same EOS. In the sub-critical regime, an oscillating NS is formed. A configuration on the dividing surface evolves towards the exact critical solution, which will oscillate forever. Configurations near the dividing surface evolve towards a solution which is nearly critical and oscillates for a long time but eventually an unstable mode sets in, driving it either collapsing to a black hole or becoming an oscillating NS.

The characteristic frequency and the central densities of the near critical solutions are significantly different from that of the oscillating NS in the sub-critical regime.

In Sec. 4.4, we determine the critical index $\gamma$ as the time scale of growth of the unstable mode bringing a near critical solution away from the critical solution. For the polytropic EOS with a polytropic index $\Gamma = 2$, commonly used to describe neutron star matter, we found $\gamma \sim 11 M_{\odot}$ with exact value depending on the rest mass and gravitational mass of the system. This corresponds to a growth time of the unstable mode of about 0.05 ms.

In Sec. 4.5, we investigate the universality of the phenomena with different critical parameter choices. Particularly interesting is the case in which the parameter is taken to be the polytropic index $\Gamma$. The same critical index is found as with other parameter choices. We point out that an adiabatic change of the EOS which can lead to a critical collapse is particularly interesting. Coupled with the facts that a solution near the critical surface will move toward the critical solution (the IA) in a short dynamical time scale, and that the unstable mode will set in a short dynamical time scale, this might enable critical collapses to be observable in nature: Upon coalescence, a hypermassive neutron star is formed, supported against gravitational collapse by angular momentum and thermal energy. Or in the case of a head-on collision, the merged object, an oscillating neutron star is formed, supported by thermal energy. The support against collapse will decrease in the dissipation/radiation time scale, which is substantially longer than the dynamical time scale of the system. This gradual loss of support can be described by an adiabatic change of the EOS, driving

the critical surface to move toward the oscillating star in the dissipation time scale. When the oscillating star is close enough to the critical surface, it will be attracted to the IA (i.e., the critical solution), until the unstable mode of the IA kicks in, and it will then collapse to a black hole through this unstable mode. This suggests that there may exist a class of gravitational collapses in nature which go through the unstable modes of a critical solution. We may observe such phenomena through the radiation characteristic of this unstable mode of the critical solution.

In Sec. 4.6, we turn to study the properties of the critical solution. We report a phase diagram of the total rest mass vs. the total ADM mass of the system. We found that the boundary line that divides the black hole and the NS solutions in this phase diagram have several branches, an interesting property that has not been seen in other critical collapse studies.

# Chapter 2

# Einstein Equations in 3+1 formalism

## 2.1 3+1 splitting of spacetime

We divide spacetime into space plus time, as the physical problem we want to deal with is an initial value problem: Given a compact object, how would it evolve? For this purpose we need to first split the representation of the spacetime into a 3+1 form, and then also split the Einstein equation into a 3+1 form.

### 2.1.1 Foliation of Spacetime

We embed a family of spacelike hyperspace $\Sigma$ such that each point on it, say (x,y,z), becomes one point in the spacetime $M$ as (t,x,y,z). We denote such a hypersurface

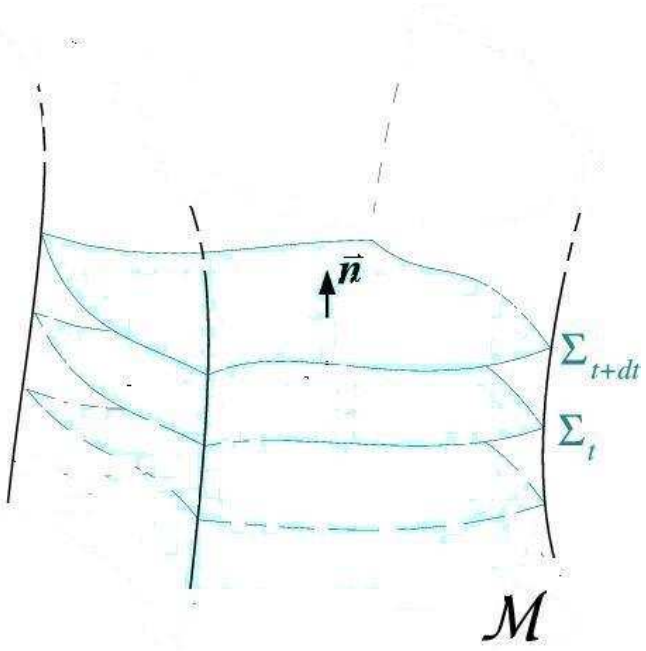


Figure 2.1: Foliation of the spacetime $\mathcal{M}$ by a family of spacelike hypersurfaces $\Sigma_t$.

as $\Sigma_t$. These surfaces are non-intersecting:

$$\Sigma_t \cap \Sigma_{t'} = \emptyset \quad \text{for } t \neq t'. \tag{2.1}$$

Each hypersurface $\Sigma_t$ is called a **slice** of the foliation, with a unit normal $\vec{n}$ as

$$\vec{n} := -N\vec{\nabla}t, \tag{2.2}$$

with

$$N := \left(-\vec{\nabla}t \cdot \vec{\nabla}t\right)^{-1/2} = \left(-\langle \mathbf{d}t, \vec{\nabla}t\rangle\right)^{-1/2}. \tag{2.3}$$

Here and in the rest of the thesis we follow the conventions of MTW [10] and Gourgoulhon [11].

We assume that all $\Sigma_t$'s are spacelike and that the foliation covers the whole $\mathbf{M}$

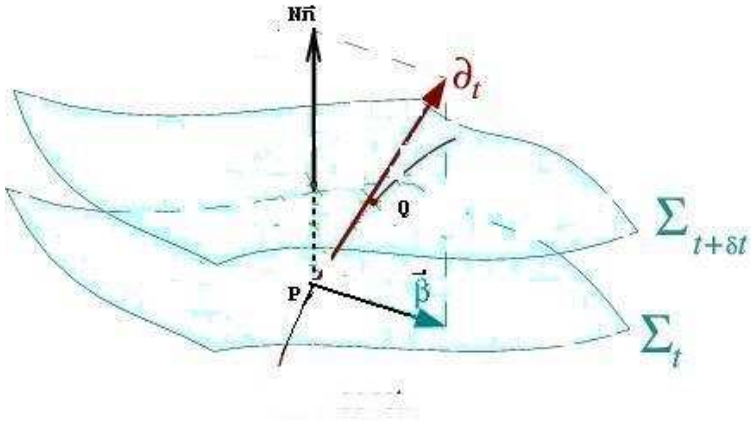


Figure 2.2: A point $P$ with coordinates $(x^i)$ on the hypersurfaces $\Sigma_t$ becomes $Q$, which has same coordinates as $P$, on the hypersurfaces on $\Sigma_{t+\delta t}$, when it is dragged along the time vector $\partial_t$. The departure is given by the shift vector $\beta$.

(cf. Fig. 2.1):

$$M = \bigcup_t \Sigma_t. \tag{2.4}$$

### 2.1.2 Shift vector

The hypersurface $\Sigma_t$ will be $\mathcal{L}ie$ dragged along $\partial_t$. Only when in very special situation the $\partial_t$ coincides with the normal evolution vector $\vec{m} = N\vec{n}$. In general we have

$$\partial_t = \vec{m} + \vec{\beta}, \tag{2.5}$$

where $\vec{\beta} =: \beta^i \partial_i$ is called the shift vector. Thus,

$$n^\alpha = \left(\frac{1}{N}, -\frac{\beta^1}{N}, -\frac{\beta^2}{N}, -\frac{\beta^3}{N}\right). \tag{2.6}$$

and because $\mathbf{n} = -N\mathbf{d}t$, we have

$$n_\alpha = (-N, 0, 0, 0). \tag{2.7}$$

And Eq. (2.5) also lead to that

$$\mathbf{n} \cdot \vec{\beta} = 0. \tag{2.8}$$

### 2.1.3 3+1 metric components

We can derive from Eq. (2.5) the time-time component of the metric tensor $\mathbf{g}$

$$g_{00} = \mathbf{g}(\partial_t, \partial_t) = \partial_t \cdot \partial_t = -N^2 + \beta \cdot \beta = -N^2 + \beta_i \beta^i, \tag{2.9}$$

and

$$g_{0i} = \mathbf{g}(\partial_t, \partial_i) = \beta \cdot \partial_i = \langle \underline{\beta}, \partial_i \rangle = \langle \beta_j \, \mathbf{d}x^j, \partial_i \rangle = \beta_i. \tag{2.10}$$

Thus the line element can now be written as

$$ds^2 = (\beta^2 - \alpha^2)dt^2 + 2\beta_i \, dt \, dx^i + \gamma_{ij} \, dx^i \, dx^j, \tag{2.11}$$

here $\gamma_{ij} = g_{ij}$ is called the induced metric on the manifold $\Sigma_t$, or the 3-metric.

### 2.1.4 Intrinsic curvature

There is a connection (or covariant derivative) $\mathbf{D}$ for the 3-metric $\gamma_{ij}$ such that

$$\mathbf{D}\gamma = 0, \tag{2.12}$$

The corresponding intrinsic curvature $R^k_{lij}$ is defined by

$$\forall \mathbf{v} \in T(\Sigma), \quad (D_i D_j - D_j D_i) v^k = R^k_{lij} v^l, \tag{2.13}$$

with the Ricci tensor in 3-D $R_{ij} = R^k_{ikj}$ and the corresponding scalar curvature as:

$$R_{ij} = \frac{\partial \Gamma^k{}_{ij}}{\partial x^k} - \frac{\partial \Gamma^k{}_{ik}}{\partial x^j} + \Gamma^k{}_{ij} \Gamma^l{}_{kl} - \Gamma^l{}_{ik} \Gamma^k{}_{lj}, \tag{2.14}$$

$$R = \gamma^{ij} R_{ij}. \tag{2.15}$$

Christoffel symbols ${\Gamma^k}_{ij}$ in terms of partial derivatives of the metric is given by

$${\Gamma^k}_{ij} = \frac{1}{2}\gamma^{kl}\left(\frac{\partial\gamma_{lj}}{\partial x^i} + \frac{\partial\gamma_{il}}{\partial x^j} - \frac{\partial\gamma_{ij}}{\partial x^l}\right). \tag{2.16}$$

### 2.1.5 The orthogonal projector

At each point $p \in \Sigma$, the space of all spacetime vectors can be orthogonally decomposed as

$$\mathcal{T}_p(\mathcal{M}) = \mathcal{T}_p(\Sigma) \oplus \mathrm{Vect}(\tilde{\mathrm{n}}), \tag{2.17}$$

where $\mathrm{Vect}(\mathbf{n})$ stands for the 1-dimensional subspace of $\mathcal{T}_p(\mathcal{M})$ generated by the vector $\mathbf{n}$.

The orthogonal projector onto $\Sigma$ from $\mathcal{M}$ is the operator $\overleftrightarrow{\gamma}$ associated with the decomposition Eq. (2.17) according to

$$\overleftrightarrow{\gamma}(\mathbf{v}) = \mathbf{v} + (\vec{n}\cdot\mathbf{v})\vec{n}. \tag{2.18}$$

It has the properties

$$\overleftrightarrow{\gamma}(\vec{n}) = 0. \tag{2.19}$$

and

$$\forall \mathbf{v} \in \mathcal{T}_p(\Sigma), \quad \overleftrightarrow{\gamma}(\mathbf{v}) = \mathbf{v}. \tag{2.20}$$

Components of $\overleftrightarrow{\gamma}$ with respect to basis $(\mathbf{e}_\alpha)$ of $\mathcal{T}_p(M)$ are

$${\gamma^\alpha}_\beta = {\delta^\alpha}_\beta + n^\alpha n_\beta. \tag{2.21}$$

By the projection operator the 3-metric can be expressed in components,

$$\gamma_{\alpha\beta} = g_{\alpha\beta} + n_\alpha n_\beta. \tag{2.22}$$

To project a general tensor from the spacetime $\mathcal{M}$ onto the hypersurface $\Sigma$ we have

$$(\overleftrightarrow{\gamma}^{*}\mathbf{T})^{\alpha_1\ldots\alpha_p}{}_{\beta_1\ldots\beta_q} = \gamma^{\alpha_1}{}_{\mu_1}\cdots\gamma^{\alpha_p}{}_{\mu_p}\gamma^{\nu_1}{}_{\beta_1}\cdots\gamma^{\nu_q}{}_{\beta_q}\,T^{\mu_1\ldots\mu_p}{}_{\nu_1\ldots\nu_q}. \tag{2.23}$$

### 2.1.6 Links between the $\nabla$ and $D$ connections

Given a tensor field $\mathbf{T}$ on $\Sigma$, its covariant derivative $\mathbf{DT}$ with respect to the Levi-Civita connection $\mathbf{D}$ of the metric $\gamma$ (cf. Sec. 2.1.4) is related to the covariant derivative $\nabla\mathbf{T}$ with respect to the spacetime connection $\nabla$ by

$$\mathbf{DT} = \overleftrightarrow{\gamma}^{*}\nabla\mathbf{T}, \tag{2.24}$$

in components [cf. Eq. (2.23)]:

$$D_\rho T^{\alpha_1\ldots\alpha_p}{}_{\beta_1\ldots\beta_q} = \gamma^{\alpha_1}{}_{\mu_1}\cdots\gamma^{\alpha_p}{}_{\mu_p}\,\gamma^{\nu_1}{}_{\beta_1}\cdots\gamma^{\nu_q}{}_{\beta_q}\,\gamma^{\sigma}{}_{\rho}\,\nabla_\sigma T^{\mu_1\ldots\mu_p}{}_{\nu_1\ldots\nu_q}. \tag{2.25}$$

### 2.1.7 Extrinsic curvature

The extrinsic curvature is related to the bending of the hypersurface $\Sigma$ in $\mathcal{M}$, defined as

$$\begin{aligned}\forall(\mathbf{u},\mathbf{v})\in\mathcal{T}_p(\mathcal{M})^2,\quad \mathbf{K}(\mathbf{u},\mathbf{v}) &= \mathbf{K}(\overleftrightarrow{\gamma}(\mathbf{u}),\overleftrightarrow{\gamma}(\mathbf{v})) = -\overleftrightarrow{\gamma}(\mathbf{u})\cdot\nabla_{\overleftrightarrow{\gamma}(\mathbf{v})}\vec{n}\\ &= -\mathbf{u}\cdot\nabla_{\mathbf{v}}\vec{n} - (\mathbf{a}\cdot\mathbf{u})(\vec{n}\cdot\mathbf{v}),\\ &= -\nabla\mathbf{n}(\mathbf{u},\mathbf{v}) - \langle\underline{\mathbf{a}},\mathbf{u}\rangle\langle\mathbf{n},\mathbf{v}\rangle,\end{aligned} \tag{2.26}$$

where we have used the fact that $\vec{n}\cdot\vec{n} = -1$ and hence $\vec{n}\cdot\nabla_{\mathbf{x}}\vec{n} = 0$ for any vector

**x**. It is valid for any pair of vectors $(\mathbf{u}, \mathbf{v})$ in $\mathcal{T}_p(\mathcal{M})$, so we conclude that

$$\nabla \mathbf{n} = -\mathbf{K} - \underline{\mathbf{a}} \otimes \mathbf{n}. \tag{2.27}$$

In component form:

$$\nabla_\beta \, n_\alpha = -K_{\alpha\beta} - a_\alpha \, n_\beta, \tag{2.28}$$

here

$$a_\mu = \frac{1}{N} \gamma^\nu_\mu \nabla_\nu N = D_\mu ln N. \tag{2.29}$$

is the 4-acceleration. Applying the projector operator $\overleftrightarrow{\gamma}^*$ to Eq. (2.27) we get:

$$\mathbf{K} = -\overleftrightarrow{\gamma}^* \nabla \mathbf{n}. \tag{2.30}$$

Taking the trace of Eq. (2.27) with respect to the metric **g** we have the trace of the extrinsic curvature tensor:

$$K = -\nabla \cdot \vec{n}. \tag{2.31}$$

By combining Eq. (2.28) and (2.29), we have

$$\nabla_\beta \, m^\alpha = -N K^\alpha{}_\beta - D^\alpha N \, n_\beta + n^\alpha \nabla_\beta N. \tag{2.32}$$

### 2.1.8 Relation between 4-D and 3-D curvatures

Since $\gamma^\nu{}_\beta n_\nu = 0$, and

$$\nabla_\mu \gamma^\sigma{}_\nu = \nabla_\mu \left( \delta^\sigma{}_\nu + n^\sigma n_\nu \right) = \nabla_\mu n^\sigma \, n_\nu + n^\sigma \nabla_\mu n_\nu,$$

according to formula (2.25)

$$\begin{aligned} D_\alpha D_\beta v^\gamma &= D_\alpha (D_\beta v^\gamma) = \gamma^\mu{}_\alpha \gamma^\nu{}_\beta \gamma^\gamma{}_\rho \nabla_\mu (D_\nu v^\rho) = \gamma^\mu{}_\alpha \gamma^\nu{}_\beta \gamma^\gamma{}_\rho \nabla_\mu \left( \gamma^\sigma{}_\nu \gamma^\rho{}_\lambda \nabla_\sigma v^\lambda \right) \\ &= -K_{\alpha\beta} \, \gamma^\gamma{}_\lambda \, n^\sigma \nabla_\sigma v^\lambda - K^\gamma{}_\alpha K_{\beta\lambda} \, v^\lambda + \gamma^\mu{}_\alpha \gamma^\sigma{}_\beta \gamma^\gamma{}_\lambda \nabla_\mu \nabla_\sigma v^\lambda, \end{aligned} \tag{2.33}$$

hence

$$D_\alpha D_\beta v^\gamma - D_\beta D_\gamma v^\gamma = \left(K_{\alpha\mu}K^\gamma{}_\beta - K_{\beta\mu}K^\gamma{}_\alpha\right) v^\mu + \gamma^\rho{}_\alpha \gamma^\sigma{}_\beta \gamma^\gamma{}_\lambda \left(\nabla_\rho \nabla_\sigma v^\lambda - \nabla_\sigma \nabla_\rho v^\lambda\right). \tag{2.34}$$

By the 3-D and 4-D Ricci identities

$$\left(K_{\alpha\mu}K^\gamma{}_\beta - K_{\beta\mu}K^\gamma{}_\alpha\right) v^\mu + \gamma^\rho{}_\alpha \gamma^\sigma{}_\beta \gamma^\gamma{}_\lambda {}^4R^\lambda{}_{\mu\rho\sigma} v^\mu = R^\gamma{}_{\mu\alpha\beta}\, v^\mu, \tag{2.35}$$

And since $\mathbf{v}$ is an arbitrary vector of $\mathcal{T}(\mathcal{M})$, we have

$$\gamma^\mu{}_\alpha \gamma^\nu{}_\beta \gamma^\gamma{}_\rho \gamma^\sigma{}_\delta {}^4R^\rho{}_{\sigma\mu\nu} = R^\gamma{}_{\delta\alpha\beta} + K^\gamma{}_\alpha K_{\delta\beta} - K^\gamma{}_\beta K_{\alpha\delta}. \tag{2.36}$$

This is the so called Gauss relation that connects the 4-D and 3-D curvatures.

We contract the Gauss relation with Eq. (2.21) to get

$$\gamma^\mu{}_\alpha \gamma^\nu{}_\beta {}^4R_{\mu\nu} + \gamma_{\alpha\mu} n^\nu \gamma^\rho{}_\beta n^\sigma {}^4R^\mu{}_{\nu\rho\sigma} = R_{\alpha\beta} + K K_{\alpha\beta} - K_{\alpha\mu}K^\mu{}_\beta. \tag{2.37}$$

We take its trace with respect to $\gamma$, take into account that $K^\mu{}_\mu = K^i{}_i = K$, $K_{\mu\nu}K^{\mu\nu} = K_{ij}K^{ij}$ to obtain

$${}^4R + 2\,{}^4R_{\mu\nu} n^\mu n^\nu = R + K^2 - K_{ij}K^{ij}. \tag{2.38}$$

This is the scalar Gauss relation, where ${}^4R$ is the 4-D curvature scalar and ${}^4R_{\mu\nu}$ is the 4-D Ricci tensor.

### 2.1.9 Lie derivative

The Lie derivative corresponds to the change determined by an observer who goes from one point $\mathbf{P}$ (coordinates $x^i$) in the direction of vector field $u^i$ to the infinitesimally neighbor point $\bar{P}$ (coordinates $x^i + \epsilon u^i(x^n)$) but still use the same coordinate

system as at point $P$. Using such a coordinate system corresponds to a coordinate transformation

$$\begin{aligned} x^{n'} &= x^n - \epsilon u^n(x^i), \\ A^{n'}_i &= \delta^n_i - \epsilon u^n_{,i}. \end{aligned} \tag{2.39}$$

The components of the vector to be considered $v^n$ at the point $\bar{P}$ will be (up to the second order in $\epsilon$)

$$\begin{aligned} v^{n'}(\bar{P}) &= A^{n'}_i v^i(x^k + \epsilon u^k) = (\delta^n_i - \epsilon u^n_{,i})[v^i(P) + \epsilon v^i_{,k}(P)u^k] \\ &= v^n(P) + \epsilon v^n_{,k}(P)u^k - \epsilon u^n_{,k} v^k(P). \end{aligned} \tag{2.40}$$

The Lie derivative of a vector field is defined as

$$\mathcal{L}_{\mathbf{u}}\, v^\alpha = v^\alpha_{,\mu} u^\mu - u^\alpha_{,\mu} v^\mu. \tag{2.41}$$

The Lie derivative of a 1-form will be similarly

$$\mathcal{L}_{\mathbf{u}}\, \omega_\alpha = \omega_{\alpha,\mu} u^\mu + u^\mu_{,\alpha} \omega_\mu. \tag{2.42}$$

We can use covariant derivative to replace the partial derivative in Eqs. (2.41) and (2.42).

$$\begin{aligned} \mathcal{L}_{\mathbf{u}}\, v^\alpha &= v^\alpha_{;\mu} u^\mu - u^\alpha_{;\mu} v^\mu, \\ \mathcal{L}_{\mathbf{u}}\, \omega_\alpha &= \omega_{\alpha;\mu} u^\mu + u^\mu_{;\alpha} \omega_\mu. \end{aligned} \tag{2.43}$$

Similarly, we can replace the partial derivatives by any connection without torsion, such as the Levi-Civita connection $\nabla$ and incorporate both vector indices, linear form indices into one tensor

$$\mathcal{L}_{\mathbf{u}}\, T^{\alpha_1\ldots\alpha_\mu}{}_{\beta_1\ldots\beta_\ell} = u^\mu \nabla_\mu T^{\alpha_1\ldots\alpha_\mu}{}_{\beta_1\ldots\beta_\ell} - \sum_{i=1}^{\mu} T^{\alpha_1\ldots \overset{i}{\downarrow} \sigma \ldots\alpha_\mu}{}_{\beta_1\ldots\beta_\ell}\, \nabla_\sigma u^{\alpha_i} + \sum_{i=1}^{\ell} T^{\alpha_1\ldots\alpha_\mu}{}_{\beta_1\ldots \underset{i}{\uparrow} \sigma \ldots\beta_\ell}\, \nabla_{\beta_i} u^\sigma. \tag{2.44}$$

## 2.2 ADM formalism of Einstein equations

### 2.2.1 Evolution of the 3-metric

The evolution of the metric $\gamma$ on $\Sigma_t$ is naturally given by the Lie derivative of $\gamma$ along the normal evolution vector $\mathbf{m}$ (see Sec. (2.1.9)). By means of Eqs. (2.44) and (2.32), we get

$$\begin{aligned}
\mathcal{L}_{\mathbf{m}}\, \gamma_{\alpha\beta} &= m^\mu \nabla_\mu \gamma_{\alpha\beta} + \gamma_{\mu\beta} \nabla_\alpha m^\mu + \gamma_{\alpha\mu} \nabla_\beta m^\mu \\
&= N n^\mu \nabla_\mu (n_\alpha n_\beta) - \gamma_{\mu\beta} \left( N K^\mu{}_\alpha + D^\mu N\, n_\alpha - n^\mu \nabla_\alpha N \right) \\
&\quad - \gamma_{\alpha\mu} \left( N K^\mu{}_\beta + D^\mu N\, n_\beta - n^\mu \nabla_\beta N \right) \\
&= -2 N K_{\alpha\beta}.
\end{aligned} \tag{2.45}$$

From the very definition of the inverse 3-metric:

$$\gamma_{ik} \gamma^{kj} = \delta^j{}_i, \tag{2.46}$$

and by using Eq. (2.45), we obtain

$$\mathcal{L}_{\mathbf{m}}\,\gamma_{ik}\,\gamma^{kj} + \gamma_{ik}\,\mathcal{L}_{\mathbf{m}}\,\gamma^{kj} = 0,$$

$$\mathcal{L}_{\mathbf{m}}\,\gamma^{ij} = 2NK^{ij},. \tag{2.47}$$

### 2.2.2 Evolution of the orthogonal projector

Let us now evaluate the Lie derivative of the orthogonal projector onto $\Sigma_t$ along the normal evolution vector. Using Eqs. (2.44) and (2.32), we have

$$\begin{aligned}
\mathcal{L}_{\mathbf{m}}\,\gamma^{\alpha}{}_{\beta} &= m^{\mu}\nabla_{\mu}\gamma^{\alpha}{}_{\beta} - \gamma^{\mu}{}_{\beta}\nabla_{\mu}m^{\alpha} + \gamma^{\alpha}{}_{\mu}\nabla_{\beta}m^{\mu} \\
&= Nn^{\mu}\nabla_{\mu}(n^{\alpha}n_{\beta}) + \gamma^{\mu}{}_{\beta}\left(NK^{\alpha}{}_{\mu} + D^{\alpha}N\,n_{\mu} - n^{\alpha}\nabla_{\mu}N\right) \\
&\quad -\gamma^{\alpha}{}_{\mu}\left(NK^{\mu}{}_{\beta} + D^{\mu}N\,n_{\beta} - n^{\mu}\nabla_{\beta}N\right) \\
&= 0.
\end{aligned} \tag{2.48}$$

Suppose $\mathbf{T}$ is a tensor field of type $\binom{1}{1}$ and is tangent to $\Sigma_t$, then

$$\gamma^{\alpha}{}_{\mu}\gamma^{\nu}{}_{\beta}T^{\mu}{}_{\nu} = T^{\alpha}{}_{\beta}. \tag{2.49}$$

Taking the Lie derivative along $\mathbf{m}$, employing the Leibniz rule and making use of Eq. (2.48) leads to

$$\mathcal{L}_{\mathbf{m}}\left(\gamma^{\alpha}{}_{\mu}\gamma^{\nu}{}_{\beta}T^{\mu}{}_{\nu}\right) = \gamma^{\alpha}{}_{\mu}\gamma^{\nu}{}_{\beta}\,\mathcal{L}_{\mathbf{m}}\,T^{\mu}{}_{\nu} = \mathcal{L}_{\mathbf{m}}\,T^{\alpha}{}_{\beta},$$

$$\overleftrightarrow{\gamma}^{*}\mathcal{L}_{\mathbf{m}}\,\mathbf{T} = \mathcal{L}_{\mathbf{m}}\,\mathbf{T}. \tag{2.50}$$

This shows that $\mathcal{L}_{\mathbf{m}}\,\mathbf{T}$ is tangent to $\Sigma_t$ if $\mathbf{T}$ is tangent to $\Sigma_t$ .

### 2.2.3 3+1 decomposition of the stress-energy tensor

We decompose the stress-energy tensor $\mathbf{T}$ as

$$\mathbf{T} = \mathbf{S} + \mathbf{n} \otimes \mathbf{p} + \mathbf{p} \otimes \mathbf{n} + E\, \mathbf{n} \otimes \mathbf{n}, \tag{2.51}$$

where

$$E := \mathbf{T}(\vec{n}, \vec{n}), \tag{2.52}$$

is the matter energy density,

$$\mathbf{p} := -\mathbf{T}(\vec{n}, \overleftrightarrow{\gamma}(.)), \tag{2.53}$$

or in component form,

$$p_\alpha = -T_{\mu\nu}\, n^\mu\, \gamma^\nu{}_\alpha, \tag{2.54}$$

is the matter momentum density, and

$$\mathbf{S} := \overleftrightarrow{\gamma}^* \mathbf{T}, \tag{2.55}$$

or in component form,

$$S_{\alpha\beta} = T_{\mu\nu} \gamma^\mu{}_\alpha \gamma^\nu{}_\beta, \tag{2.56}$$

is the matter stress tensor. Given two spacelike unit vectors $\mathbf{e}$ and $\mathbf{e}'$ in the rest frame of the Eulerian observer (both vectors are orthogonal to $\mathbf{n}$), $S(\mathbf{e}, \mathbf{e}')$ is the force in the direction $\mathbf{e}$ acting on the unit surface whose normal is $\mathbf{e}'$. The trace of $\mathbf{S}$ with respect to the metric $\gamma$ (or equivalently with respect to the metric $\mathbf{g}$) is defined as:

$$S := \gamma^{ij} S_{ij} = g^{\mu\nu} S_{\mu\nu}. \tag{2.57}$$

Taking the trace of Eq. (2.51) with respect to the metric $\mathbf{g}$ yields

$$T = S - E. \tag{2.58}$$

For a perfect fluid model of matter we have

$$\mathbf{T} = (\rho + P)\,\mathbf{u} \otimes \mathbf{u} + P\,\mathbf{g}, \tag{2.59}$$

where $\mathbf{u}$ is the 4-velocity of a fluid element, $\rho$ and $P$ are two scalar fields, representing respectively the matter energy density and the isotropic pressure, both measured in the fluid frame (i.e. by an observer who is comoving with the fluid).

### 2.2.4 Evolution of the Extrinsic Curvature

By projection twice onto $\Sigma_t$ and once along $\mathbf{n}$ of the 4-D Ricci identity, using of Eq. (2.28), we arrive at

$$\begin{aligned}
\gamma_{\alpha\mu}\, n^\rho \gamma^\nu{}_\beta\, n^\sigma\, {}^4R^\mu{}_{\rho\nu\sigma} &= \gamma_{\alpha\mu} n^\sigma \gamma^\nu{}_\beta (\nabla_\nu \nabla_\sigma n^\mu - \nabla_\sigma \nabla_\nu n^\mu) \\
&= \gamma_{\alpha\mu} n^\sigma \gamma^\nu{}_\beta \left[-\nabla_\nu (K^\mu{}_\sigma + D^\mu \ln N\; n_\sigma) + \nabla_\sigma (K^\mu{}_\nu + D^\mu \ln N\; n_\nu)\right] \\
&= -K_{\alpha\sigma} K^\sigma{}_\beta + \frac{1}{N} D_\beta D_\alpha N + \gamma^\mu{}_\alpha \gamma^\nu{}_\beta\, n^\sigma \nabla_\sigma K_{\mu\nu}.
\end{aligned} \tag{2.60}$$

And by Eq. 2.44 we have

$$\begin{aligned}
\mathcal{L}_{\mathbf{m}} K_{\alpha\beta} &= m^\mu \nabla_\mu K_{\alpha\beta} + K_{\mu\beta} \nabla_\alpha m^\mu + K_{\alpha\mu} \nabla_\beta m^\mu \\
&= N n^\mu \nabla_\mu K_{\alpha\beta} - 2N K_{\alpha\mu} K^\mu{}_\beta - K_{\alpha\mu} D^\mu N\; n_\beta - K_{\beta\mu} D^\mu N\; n_\alpha.
\end{aligned} \tag{2.61}$$

We project this equation onto $\Sigma_t$, i.e. apply the operator $\overleftrightarrow{\gamma}^*$ to both sides and note that $\mathcal{L}_{\mathbf{m}}\,\mathbf{K}$ is tangent to $\Sigma_t$ (since $\mathbf{K}$ is), then

$$\mathcal{L}_{\mathbf{m}} K_{\alpha\beta} = N\, \gamma^\mu{}_\alpha \gamma^\nu{}_\beta\, n^\sigma \nabla_\sigma K_{\mu\nu} - 2N K_{\alpha\mu} K^\mu{}_\beta. \tag{2.62}$$

Plugging it into Eq. (2.60) and combining with the contracted Gauss relation Eq. (2.37) we have

$$\gamma^{\mu}{}_{\alpha}\gamma^{\nu}{}_{\beta}\,{}^{4}R_{\mu\nu} = -\frac{1}{N}\mathcal{L}_{\mathbf{m}}\,K_{\alpha\beta} - \frac{1}{N}D_{\alpha}D_{\beta}N + R_{\alpha\beta} + KK_{\alpha\beta} - 2K_{\alpha\mu}K^{\mu}{}_{\beta}. \tag{2.63}$$

Now we project the Einstein equations onto $\Sigma_t$

$$\overleftrightarrow{\gamma}^{*}\,{}^{4}\mathbf{R} = 8\pi\left(\overleftrightarrow{\gamma}^{*}\mathbf{T} - \frac{1}{2}T\,\overleftrightarrow{\gamma}^{*}\mathbf{g}\right). \tag{2.64}$$

Combining Eqs. (2.63) and (2.64), and notes that $\overleftrightarrow{\gamma}^{*}\mathbf{T}$ is by definition $\mathbf{S}$, $T = S - E$ [Eq. (2.58)], and $\overleftrightarrow{\gamma}^{*}\mathbf{g}$ is simply $\gamma$, therefore

$$\mathcal{L}_{\mathbf{m}}\,\mathbf{K} = -\mathbf{D}\mathbf{D}N + N\left\{\mathbf{R} + K\mathbf{K} - 2\mathbf{K}\cdot\vec{\mathbf{K}} + 4\pi\left[(S-E)\gamma - 2\mathbf{S}\right]\right\}. \tag{2.65}$$

In component form,

$$\mathcal{L}_{\mathbf{m}}\,K_{\alpha\beta} = -D_{\alpha}D_{\beta}N + N\left\{R_{\alpha\beta} + KK_{\alpha\beta} - 2K_{\alpha\mu}K^{\mu}{}_{\beta} + 4\pi\left[(S-E)\gamma_{\alpha\beta} - 2S_{\alpha\beta}\right]\right\}. \tag{2.66}$$

Let us take the trace of Eq. (2.63) with $\gamma^{\alpha\beta}$. Note that in the right-hand side we can limit the range of variation of the indices to $\{1,2,3\}$ since all the involved tensors are spatial ones [including $\mathcal{L}_{\mathbf{m}}\,\mathbf{K}$]. Hence

$$\gamma^{\mu\nu}\,{}^{4}R_{\mu\nu} = -\frac{1}{N}\gamma^{ij}\mathcal{L}_{\mathbf{m}}\,K_{ij} - \frac{1}{N}D_{i}D^{i}N + R + K^{2} - 2K_{ij}K^{ij}. \tag{2.67}$$

Now $\gamma^{\mu\nu}\,{}^{4}R_{\mu\nu} = (g^{\mu\nu} + n^{\mu}n^{\nu})\,{}^{4}R_{\mu\nu} = {}^{4}R + {}^{4}R_{\mu\nu}n^{\mu}n^{\nu}$ and

$$\begin{aligned} -\gamma^{ij}\mathcal{L}_{\mathbf{m}}\,K_{ij} &= -\mathcal{L}_{\mathbf{m}}\,(\underbrace{\gamma^{ij}K_{ij}}_{=K}) + K_{ij}\mathcal{L}_{\mathbf{m}}\,\gamma^{ij} \\ &= -\mathcal{L}_{\mathbf{m}}\,K + 2NK_{ij}K^{ij} \end{aligned} \tag{2.68}$$

Combine the scalar Gauss relation (2.38), Eq. (2.67) and (2.68) we arrive

$$ {}^4R = R + K^2 + K_{ij}K^{ij} - \frac{2}{N}\mathcal{L}_{\mathbf{m}}\, K - \frac{2}{N} D_i D^i N. \tag{2.69} $$

### 2.2.5 Constraints equations

We first project the Einstein equation fully perpendicular to $\Sigma_t$

$$ {}^4\mathbf{R}(\vec{n},\vec{n}) + \frac{1}{2}{}^4R = 8\pi \mathbf{T}(\vec{n},\vec{n}). \tag{2.70} $$

here we have used $\mathbf{g}(\vec{n},\vec{n}) = -1$. Notice that $\mathbf{T}(\vec{n},\vec{n}) = E$, we arrive that

$$ R + K^2 - K_{ij}K^{ij} = 16\pi E. \tag{2.71} $$

This equation is called the Hamiltonian constraint.

Now, let us project the Einstein equation once onto $\Sigma_t$ and once along the normal $\vec{n}$:

$$ {}^4\mathbf{R}(\vec{n},\overleftrightarrow{\gamma}(.)) - \frac{1}{2}{}^4R\,\underbrace{\mathbf{g}(\vec{n},\overleftrightarrow{\gamma}(.))}_{=0} = 8\pi \mathbf{T}(\vec{n},\overleftrightarrow{\gamma}(.)) = -\mathbf{p}. \tag{2.72} $$

Now, from Eq. (2.28),

$$ \begin{aligned} \gamma^\mu{}_\alpha \gamma^\nu{}_\beta \gamma^\gamma{}_\rho \nabla_\mu \nabla_\nu n^\rho &= \gamma^\mu{}_\alpha \gamma^\nu{}_\beta \gamma^\gamma{}_\rho \nabla_\mu \left(-K^\rho{}_\nu - a^\rho n_\nu\right) \\ &= -D_\alpha K^\gamma{}_\beta + a^\gamma K_{\alpha\beta}, \end{aligned} \tag{2.73} $$

Project the Ricci identity

$$ \left(\nabla_\alpha \nabla_\beta - \nabla_\beta \nabla_\alpha\right) n^\gamma = {}^4R^\gamma{}_{\mu\alpha\beta}\, n^\mu. \tag{2.74} $$

onto $\Sigma_t$ we have

$$ \gamma^\gamma{}_\rho\, n^\sigma\, \gamma^\mu{}_\alpha \gamma^\nu{}_\beta\, {}^4R^\rho{}_{\sigma\mu\nu} = D_\beta K^\gamma{}_\alpha - D_\alpha K^\gamma{}_\beta. \tag{2.75} $$

Contracting over indices $\alpha$ and $\gamma$, we have

$$\gamma^{\mu}{}_{\alpha} n^{\nu}\, {}^{4}R_{\mu\nu} = D_{\alpha}K - D_{\mu}K^{\mu}{}_{\alpha}. \tag{2.76}$$

Combine Eqs. (2.72) and (2.76), we derive

$$D_j K^j{}_i - D_i K = 8\pi p_i. \tag{2.77}$$

This equation is called the momentum constraint.

Hamiltonian and momentum constraints are relations that must be satisfied in each time slice for a physical spacetime.

### 2.2.6 3+1 Einstein evolution equation system

Notice that each term in Eq. (2.66) is a tensor field tangent to $\Sigma_t$. Consequently, we may restrict to spatial indices without any loss of generality. Put it together with Eq. (2.47), (2.71) and (2.77), we rewrite the 3+1 Einstein evolution system as

$$\left(\frac{\partial}{\partial t} - \mathcal{L}_{\beta}\right)\gamma_{ij} = -2NK_{ij}, \tag{2.78}$$

$$\left(\frac{\partial}{\partial t} - \mathcal{L}_{\beta}\right)K_{ij} = -D_i D_j N + N\left\{R_{ij} + KK_{ij} - 2K_{ik}K^{k}{}_{j} + 4\pi\left[(S-E)\gamma_{ij} - 2S_{ij}\right]\right\}, \tag{2.79}$$

together with the constraint equations

$$R + K^2 - K_{ij}K^{ij} = 16\pi E, \tag{2.80}$$

$$D_j K^j{}_i - D_i K = 8\pi p_i. \tag{2.81}$$

We completed the splitting of the Einstein equation into a 3+1 formulation, with 4 constraint equations to be satisfied for each time slice, and 6 evolution equations to evolve from one time slice to the next.

### 2.2.7 3+1 equations for the matter fields

Next we split the hydrodynamic equations into a 3+1 form.

The baryon number conservation of the matter leads to

$$\nabla \cdot \mathbf{j}_{\mathrm{B}} = 0, \tag{2.82}$$

where

$$\mathbf{j}_{\mathrm{B}} = n_{\mathrm{B}}\mathbf{u}, \tag{2.83}$$

is the baryon number 4-current, here $\mathbf{u}$ is the fluid 4-velocity and $n_{\mathrm{B}}$ the fluid proper baryon number density.

Introduce the fluid velocity relative to the Eulerian observer (in $\vec{n}$ direction) as $\mathbf{U}$, we have

$$\mathbf{u} = \Gamma(\vec{n} + \mathbf{U}), \tag{2.84}$$

with $\vec{n} \cdot \mathbf{U} = 0$, $\vec{n} \cdot \vec{n} = -1$ and $\mathbf{u} \cdot \mathbf{u} = -1$,

$$\Gamma = (1 - \mathbf{U} \cdot \mathbf{U})^{-1/2}. \tag{2.85}$$

And we have

$$\mathbf{U} = \frac{1}{N}(\mathbf{V} + \beta), \tag{2.86}$$

here

$$V^i = \frac{dx^i}{dt} = \frac{u^i}{u^0}. \tag{2.87}$$

Then Eq. (2.82) becomes

$$\begin{aligned} 0 &= \partial_0[N\sqrt{\gamma}\rho_0 u^0] + \partial_i[N\sqrt{\gamma}\rho_0\Gamma(n^i + U^i)] \\ &= \partial_0[\sqrt{\gamma}\rho_0\Gamma] + \partial_i[\sqrt{\gamma}\rho_0\Gamma V^i], \end{aligned} \tag{2.88}$$

here $\rho_0 = m_B n_B$ is the baryon density with $m_B$ the baryon mass. On the other hand, due to the contracted Bianchi identities, we have for the energy-momentum tensor $\mathbf{T}^{\mu\nu}$,

$$0 = \nabla_\mu T^\mu{}_\alpha = \nabla_\mu \left(S^\mu{}_\alpha + n^\mu p_\alpha + p^\mu n_\alpha + E n^\mu n_\alpha\right). \tag{2.89}$$

For $\alpha = 0$, we have the energy conservation equation as

$$\left(\frac{\partial}{\partial t} - \beta^i \frac{\partial}{\partial x^i}\right) E + N\left(D_i p^i - KE - K_{ij}S^{ij}\right) + 2p^i D_i N = 0. \tag{2.90}$$

On the other hand, the momentum conservation comes with the spatial components of Eq. (2.89)

$$\left(\frac{\partial}{\partial t} - \mathcal{L}_\beta\right) p_i + N D_j S^j{}_i + S_{ij} D^j N - NK p_i + E D_i N = 0. \tag{2.91}$$

## 2.3 Conformal decomposition

While Eq. (2.78) and (2.79) can be used for numerical evolution, in order to get a stable evolution, rewriting the equations into the following forms separating out the conformal degree of freedom is useful.

### 2.3.1 Conformal metric

Define a conformal metric as

$$\tilde{\gamma}_{\mathbf{ij}} := \Psi^{-4}\gamma_{ij}, \tag{2.92}$$

Then the inverse conformal metric $\tilde{\gamma}^{ij}$ is given by the requirement

$$\tilde{\gamma}_{ik}\,\tilde{\gamma}^{kj} = \delta_i{}^j, \tag{2.93}$$

which is equivalent to

$$\tilde{\gamma}^{ij} = \Psi^4\,\gamma^{ij}. \tag{2.94}$$

### 2.3.2 Conformal connection

$\tilde{\gamma}$ being a well defined metric on $\Sigma_t$, let $\tilde{\mathbf{D}}$ be the Levi-Civita connection associated to it:

$$\tilde{\mathbf{D}}\tilde{\gamma} = 0. \tag{2.95}$$

Let us denote by $\tilde{\Gamma}^k{}_{ij}$ the Christoffel symbols of $\tilde{\mathbf{D}}$ with respect to the coordinates $(x^i)$:

$$\tilde{\Gamma}^k{}_{ij} = \frac{1}{2}\tilde{\gamma}^{kl}\left(\frac{\partial\tilde{\gamma}_{lj}}{\partial x^i} + \frac{\partial\tilde{\gamma}_{il}}{\partial x^j} - \frac{\partial\tilde{\gamma}_{ij}}{\partial x^l}\right). \tag{2.96}$$

The covariant derivatives $\tilde{\mathbf{D}}\mathbf{T}$ and $\mathbf{D}\mathbf{T}$ for a tensor field $\mathbf{T}$ of type $\binom{p}{q}$ on $\Sigma_t$ are related by

$$D_k T^{i_1\ldots i_p}{}_{j_1\ldots j_q} = \tilde{D}_k T^{i_1\ldots i_p}{}_{j_1\ldots j_q} + \sum_{r=1}^{p} C^{i_r}{}_{kl}\,T^{i_1\ldots l\ldots i_p}{}_{j_1\ldots j_q} - \sum_{r=1}^{q} C^{l}{}_{kj_r}\,T^{i_1\ldots i_p}{}_{j_1\ldots l\ldots j_q}, \tag{2.97}$$

where

$$C^k{}_{ij} := \Gamma^k{}_{ij} - \tilde{\Gamma}^k{}_{ij}, \tag{2.98}$$

$\Gamma^k{}_{ij}$ being the Christoffel symbols of the connection $\mathbf{D}$.

It is easy to verify that

$$C^k{}_{ij} = \frac{1}{2}\gamma^{kl}\left(\tilde{D}_i\gamma_{lj} + \tilde{D}_j\gamma_{il} - \tilde{D}_l\gamma_{ij}\right). \tag{2.99}$$

Replacing $\gamma_{ij}$ and $\gamma^{ij}$ in terms of $\tilde{\gamma}_{ij}$, $\tilde{\gamma}^{ij}$ and $\Psi$ we can finally arrive at:

$$C^k{}_{ij} = 2\left(\delta^k{}_i\tilde{D}_j \ln\Psi + \delta^k{}_j\tilde{D}_i \ln\Psi - \tilde{D}^k \ln\Psi\, \tilde{\gamma}_{ij}\right). \tag{2.100}$$

For a vector we have as a special case of Eq. (2.97),

$$D_i v^i = \Psi^{-6}\tilde{D}_i\left(\Psi^6 v^i\right). \tag{2.101}$$

### 2.3.3 Expression of the Ricci tensor

Expressing the $\mathbf{D}$-derivatives in term of the $\tilde{\mathbf{D}}$-derivatives in

$$R_{ij}v^j = D_jD_iv^j - D_iD_jv^j, \tag{2.102}$$

and noting that the corresponding formula for the conformal quantities

$$\tilde{D}_j\tilde{D}_iv^j - \tilde{D}_i\tilde{D}_jv^j = \tilde{R}_{ij}v^j, \tag{2.103}$$

we can derive

$$R_{ij} = \tilde{R}_{ij} + \tilde{D}_kC^k{}_{ij} - \tilde{D}_iC^k{}_{kj} + C^k{}_{ij}C^l{}_{lk} - C^k{}_{il}C^l{}_{kj}, \tag{2.104}$$

or in term of the conformal factor

$$R_{ij} = \tilde{R}_{ij} - 2\tilde{D}_i\tilde{D}_j \ln\Psi - 2\tilde{D}_k\tilde{D}^k \ln\Psi\, \tilde{\gamma}_{ij} + 4\tilde{D}_i \ln\Psi\, \tilde{D}_j \ln\Psi - 4\tilde{D}_k \ln\Psi\, \tilde{D}^k \ln\Psi\, \tilde{\gamma}_{ij}, \tag{2.105}$$

and

$$R = \Psi^{-4}\tilde{R} - 8\Psi^{-5}\tilde{D}_i\tilde{D}^i\Psi. \tag{2.106}$$

### 2.3.4 Conformal decomposition of the extrinsic curvature

Let us first decompose the extrinsic curvature as

$$K_{ij} = A_{ij} + \frac{1}{3}K\gamma_{ij} \qquad \text{and} \qquad K^{ij} = A^{ij} + \frac{1}{3}K\gamma^{ij}. \tag{2.107}$$

where

$$\mathrm{tr}_\gamma\, \mathbf{A} = \gamma^{ij}A_{ij} = 0. \tag{2.108}$$

The conformal scaling for time evolution is

$$A^{ij} = \Psi^{-4}\tilde{A}^{ij}, \tag{2.109}$$

and

$$A_{ij} := \Psi^4\tilde{A}_{ij}. \tag{2.110}$$

Besides,

$$K_{ij}K^{ij} = \left(A_{ij} + \frac{K}{3}\gamma_{ij}\right)\left(A^{ij} + \frac{K}{3}\gamma^{ij}\right) = A_{ij}A^{ij} + \frac{K^2}{3} = \tilde{A}_{ij}\tilde{A}^{ij} + \frac{K^2}{3}. \tag{2.111}$$

### 2.3.5 Conformal decomposition of the Einstein equations

From Eq. (2.78) we arrive

$$\mathcal{L}_{\mathbf{m}}\,\tilde{\gamma}_{ij} = -2N\Psi^{-4}A_{ij} - \frac{2}{3}\left(NK + 6\mathcal{L}_{\mathbf{m}}\,\ln\Psi\right)\tilde{\gamma}_{ij}. \tag{2.112}$$

Take trace , note that $\mathbf{A}_{ij}$ is traceless, and

$$\delta(\ln\det A) = \mathrm{tr}(A^{-1}\times\delta A), \tag{2.113}$$

$$-2(NK + 6\mathcal{L}_{\mathbf{m}}\,\ln\Psi) = \tilde{\gamma}^{ij}\mathcal{L}_{\mathbf{m}}\,\tilde{\gamma}_{ij} = \mathcal{L}_{\mathbf{m}}\,\ln\det(\tilde{\gamma}_{ij}). \tag{2.114}$$

By construction, $\det(\tilde{\gamma}_{ij}) = \det f_{ij} = f$ ($f_{ij}$ is the flat metric), and $\partial f/\partial t = 0$,

$$\begin{aligned}\mathcal{L}_{\mathbf{m}}\,\ln\det(\tilde{\gamma}_{ij}) &= -\mathcal{L}_{\beta}\,\ln f = -\mathcal{L}_{\beta}\,\ln\det(\tilde{\gamma}_{ij})\\ &= -\tilde{\gamma}^{ij}\mathcal{L}_{\beta}\,\tilde{\gamma}_{ij} = -2\tilde{D}_i\beta^i.\end{aligned} \tag{2.115}$$

Combine with Eq. (2.114) we get the equation for the conformal factor

$$\left(\frac{\partial}{\partial t} - \mathcal{L}_{\beta}\right)\ln\Psi = \frac{1}{6}\left(\tilde{D}_i\beta^i - NK\right). \tag{2.116}$$

Insert it into Eq. (2.112), we have

$$\left(\frac{\partial}{\partial t} - \mathcal{L}_{\beta}\right)\tilde{\gamma}_{ij} = -2N\tilde{A}_{ij} - \frac{2}{3}\tilde{D}_k\beta^k\,\tilde{\gamma}_{ij}. \tag{2.117}$$

Accordingly we can derive

$$\left(\frac{\partial}{\partial t} - \mathcal{L}_{\beta}\right)\tilde{\gamma}^{ij} = 2N\tilde{A}^{ij} + \frac{2}{3}\tilde{D}_k\beta^k\,\tilde{\gamma}^{ij}. \tag{2.118}$$

Take the trace of Eq. (2.79) we have

$$\begin{aligned}\mathcal{L}_{\mathbf{m}}\,K &= \gamma^{ij}\mathcal{L}_{\mathbf{m}}\,K_{ij} + 2NK_{ij}K^{ij}\\ &= -D_iD^iN + N\left[R + K^2 + 4\pi(S - 3E)\right].\end{aligned} \tag{2.119}$$

By using of the Hamiltonian constraints Eq. (2.79),

$$\left(\frac{\partial}{\partial t} - \mathcal{L}_\beta\right) K = -D_i D^i N + N\left[4\pi(E+S) + A_{ij}A^{ij} + \frac{K^2}{3}\right]. \tag{2.120}$$

Taking **Lie** derivative of Eq. (2.107)

$$\mathcal{L}_{\mathbf{m}}\, K_{ij} = \mathcal{L}_{\mathbf{m}}\, A_{ij} + \frac{1}{3}\mathcal{L}_{\mathbf{m}}\, K\, \gamma_{ij} - \frac{2}{3} K N K_{ij}. \tag{2.121}$$

replacing $K_{ij}$ by $A_{ij}$ we have

$$\begin{aligned}\mathcal{L}_{\mathbf{m}}\, A_{ij} &= -D_i D_j N + N\left[R_{ij} + \frac{1}{3}KA_{ij} - 2A_{ik}A^k{}_j - 8\pi\left(S_{ij} - \frac{1}{3}S\gamma_{ij}\right)\right] \\ &\quad + \frac{1}{3}\left(D_k D^k N - NR\right)\gamma_{ij}.\end{aligned} \tag{2.122}$$

The corresponding conformal version of Eqs. (2.120) and (2.122) are

$$\left(\frac{\partial}{\partial t} - \mathcal{L}_\beta\right) K = -\Psi^{-4}\left(\tilde{D}_i\tilde{D}^i N + 2\tilde{D}_i \ln\Psi\, \tilde{D}^i N\right) + N\left[4\pi(E+S) + \tilde{A}_{ij}\tilde{A}^{ij} + \frac{K^2}{3}\right], \tag{2.123}$$

and

$$\begin{aligned}\left(\frac{\partial}{\partial t} - \mathcal{L}_\beta\right)\tilde{A}_{ij} &= -\frac{2}{3}\tilde{D}_k\beta^k\,\tilde{A}_{ij} + N\left[K\tilde{A}_{ij} - 2\tilde{\gamma}^{kl}\tilde{A}_{ik}\tilde{A}_{jl} - 8\pi\left(\Psi^{-4}S_{ij} - \frac{1}{3}S\tilde{\gamma}_{ij}\right)\right] \\ &\quad + \Psi^{-4}\Big\{ - \tilde{D}_i\tilde{D}_j N + 2\tilde{D}_i \ln\Psi\, \tilde{D}_j N + 2\tilde{D}_j \ln\Psi\, \tilde{D}_i N \\ &\qquad + \frac{1}{3}\left(\tilde{D}_k\tilde{D}^k N - 4\tilde{D}_k \ln\Psi\, \tilde{D}^k N\right)\tilde{\gamma}_{ij} \\ &\qquad + N\Big[\tilde{R}_{ij} - \frac{1}{3}\tilde{R}\tilde{\gamma}_{ij} - 2\tilde{D}_i\tilde{D}_j \ln\Psi + 4\tilde{D}_i \ln\Psi\, \tilde{D}_j \ln\Psi \\ &\qquad\quad + \frac{2}{3}\left(\tilde{D}_k\tilde{D}^k \ln\Psi - 2\tilde{D}_k \ln\Psi\, \tilde{D}^k \ln\Psi\right)\tilde{\gamma}_{ij}\Big]\Big\}.\end{aligned} \tag{2.124}$$

### 2.3.6 Conformal decomposition of the constraints equations

Substituting Eq. (2.106) for $R$ and Eq. (2.111) into the Hamiltonian constraint equation (2.80) yields

$$\tilde{D}_i\tilde{D}^i\Psi - \frac{1}{8}\tilde{R}\Psi + \left(\frac{1}{8}\tilde{A}_{ij}\tilde{A}^{ij} - \frac{1}{12}K^2 + 2\pi E\right)\Psi^5 = 0. \tag{2.125}$$

Let us first express the momentum constraint in terms of $A^{ij}$. Note that

$$D_jK^{ij} = D_jA^{ij} + \frac{1}{3}D^iK. \tag{2.126}$$

Taking into account relation (2.109), we can easily rewrite Eq. (2.81) in terms of $\tilde{A}^{ij}$:

$$\tilde{D}_j\tilde{A}^{ij} + 6\tilde{A}^{ij}\tilde{D}_j\ln\Psi - \frac{2}{3}\tilde{D}^iK = 8\pi\Psi^4p^i. \tag{2.127}$$

### 2.3.7 Summary: conformal 3+1 Einstein system

Let us gather Eqs. (2.116), (2.117), (2.123), (2.124), (2.125) and (2.127):

$$\left(\frac{\partial}{\partial t}-\mathcal{L}_\beta\right)\Psi=\frac{\Psi}{6}\left(\tilde{D}_i\beta^i-NK\right) \tag{2.128}$$

$$\left(\frac{\partial}{\partial t}-\mathcal{L}_\beta\right)\tilde{\gamma}_{ij}=-2N\tilde{A}_{ij}-\frac{2}{3}\tilde{D}_k\beta^k\,\tilde{\gamma}_{ij} \tag{2.129}$$

$$\left(\frac{\partial}{\partial t}-\mathcal{L}_\beta\right)K=-\Psi^{-4}\left(\tilde{D}_i\tilde{D}^iN+2\tilde{D}_i\ln\Psi\,\tilde{D}^iN\right)+N\left[4\pi(E+S)+\tilde{A}_{ij}\tilde{A}^{ij}+\frac{K^2}{3}\right] \tag{2.130}$$

$$\begin{aligned}\left(\frac{\partial}{\partial t}-\mathcal{L}_\beta\right)\tilde{A}_{ij} &= -\frac{2}{3}\tilde{D}_k\beta^k\,\tilde{A}_{ij}+N\left[K\tilde{A}_{ij}-2\tilde{\gamma}^{kl}\tilde{A}_{ik}\tilde{A}_{jl}-8\pi\left(\Psi^{-4}S_{ij}-\frac{1}{3}S\tilde{\gamma}_{ij}\right)\right]\\ &\quad+\Psi^{-4}\Big\{-\tilde{D}_i\tilde{D}_jN+2\tilde{D}_i\ln\Psi\,\tilde{D}_jN+2\tilde{D}_j\ln\Psi\,\tilde{D}_iN\\ &\quad+\frac{1}{3}\left(\tilde{D}_k\tilde{D}^kN-4\tilde{D}_k\ln\Psi\,\tilde{D}^kN\right)\tilde{\gamma}_{ij}\\ &\quad+N\Big[\tilde{R}_{ij}-\frac{1}{3}\tilde{R}\tilde{\gamma}_{ij}-2\tilde{D}_i\tilde{D}_j\ln\Psi+4\tilde{D}_i\ln\Psi\,\tilde{D}_j\ln\Psi\\ &\quad+\frac{2}{3}\left(\tilde{D}_k\tilde{D}^k\ln\Psi-2\tilde{D}_k\ln\Psi\,\tilde{D}^k\ln\Psi\right)\tilde{\gamma}_{ij}\Big]\Big\}.\end{aligned} \tag{2.131}$$

$$\tilde{D}_i\tilde{D}^i\Psi-\frac{1}{8}\tilde{R}\Psi+\left(\frac{1}{8}\tilde{A}_{ij}\tilde{A}^{ij}-\frac{1}{12}K^2+2\pi E\right)\Psi^5=0 \tag{2.132}$$

$$\tilde{D}_j\tilde{A}^{ij}+6\tilde{A}^{ij}\tilde{D}_j\ln\Psi-\frac{2}{3}\tilde{D}^iK=8\pi\Psi^4p^i. \tag{2.133}$$

This is the set of spacetime evolution equations and constraint equations on which we base our numerical study.

## 2.4 Gauge choices

One of the hardest problems in numerical evolution of the Einstein system is to make good gauge choices responding to the geometry, which is dynamical.

### 2.4.1 Choice of foliation

#### Geodesic slicing

This corresponds to the condition

$$N = 1. \tag{2.134}$$

This implies that the 4-acceleration of the Eulerian observers [that's just the spatial gradient of $\ln N$ (cf. Eq. (2.29))] $\mathbf{a} = 0$, i.e. the worldlines of the Eulerian observers are geodesics. Moreover the choice (2.134) implies that the proper time along these worldlines coincides with the coordinate time $t$. This simple choice often leads to the development of coordinate singularity.

#### Maximal slicing

The maximal slicing corresponds to the vanishing of the mean curvature of the hypersurfaces $\Sigma_t$:

$$K = 0. \tag{2.135}$$

and this condition leads to hypersurfaces of *maximal volume*.

Besides its nice geometrical definition, an interesting property of maximal slicing is its singularity avoidance property. This is related to the fact that the set of the Eulerian observers of a maximal foliation define an *incompressible flow*: from Eq. (2.31), the condition $K = 0$ is equivalent to the incompressibility condition

$$\nabla \cdot \vec{n} = 0 \tag{2.136}$$

for the 4-velocity field $\vec{n}$ of the Eulerian observers. The maximal slice provides stability. But unfortunately it involves the solving of a elliptical equation which is computationally expensive.

**Harmonic slicing**

We say a coordinate $(x^\alpha)$ is harmonic if the following equation holds

$$\Box_{\mathbf{g}} x^\alpha = 0, \tag{2.137}$$

where $\Box_{\mathbf{g}} := \nabla_\mu \nabla^\mu$ is the d'Alembertian associated with the metric $\mathbf{g}$. The **harmonic slicing** is defined when this condition holds for $x^0 = t$ (but not necessarily for the other coordinates, leaving the freedom to choose any coordinate $(x^i)$ in each hypersurface $\Sigma_t$). Using the standard expression for the d'Alembertian, it means that

$$\frac{1}{\sqrt{-g}} \frac{\partial}{\partial x^\mu} \left( \sqrt{-g} g^{\mu\nu} \underbrace{\frac{\partial t}{\partial x^\nu}}_{=\delta^0{}_\nu} \right) = 0, \tag{2.138}$$

Insert the metric components,

$$-\frac{\partial}{\partial t} \left( \frac{\sqrt{\gamma}}{N} \right) + \frac{\partial}{\partial x^i} \left( \frac{\sqrt{\gamma}}{N} \beta^i \right) = 0. \tag{2.139}$$

The final result can be written as:

$$\left( \frac{\partial}{\partial t} - \mathcal{L}_\beta \right) N = -KN^2. \tag{2.140}$$

This slicing is singularity avoiding, however it is less stable than the maximal slicing.

**1+log slicing**

The harmonic slicing condition (2.140) has been generalized to

$$\left(\frac{\partial}{\partial t} - \mathcal{L}_\beta\right) N = -KN^2 f(N), \tag{2.141}$$

where $f$ is an arbitrary function. The harmonic slicing corresponds to $f(N) = 1$. The geodesic slicing also fulfills this relation with $f(N) = 0$. The choice $f(N) = 2/N$ leads to

$$\left(\frac{\partial}{\partial t} - \mathcal{L}_\beta\right) N = -2KN. \tag{2.142}$$

a solution of which is

$$N = 1 + \ln \gamma. \tag{2.143}$$

For this reason, a foliation whose lapse function obeys Eq. (2.142) is called a **$1 + \log$ slicing**. This slicing is also singularity avoiding. It is expressed algebraically locally, and hence easy to implement. This is the slicing most commonly used in our numerical simulations.

## 2.5 Evolution of spatial coordinates

This section discusses choices of $\beta$ which setup coordinates on slices $\mathbf{\Sigma}_t$.

### 2.5.1 Normal coordinates

As for the lapse choice $N = 1$ (geodesic slicing, Sec. 2.4.1), the simplest choice for the shift vector is to set it to zero:

$$\beta = 0. \tag{2.144}$$

Besides their simplicity, an advantage of normal coordinates is to be as regular as the foliation itself: they cannot introduce some pathology per themselves. On the other hand, the major drawback of these coordinates is that they may lead to a large coordinate shear, resulting in large values of the metric coefficients $\gamma_{ij}$. This is especially true if rotation is present.

### 2.5.2 Minimal distortion

The distortion tensor $\mathbf{Q}$ is defined as the trace-free part of the time derivative of the physical metric $\gamma$:

$$Q_{ij} = \frac{\partial \gamma_{ij}}{\partial t} - \frac{1}{3}\gamma^{kl}\frac{\partial \gamma_{kl}}{\partial t}\,\gamma_{ij} = \Psi^4 \frac{\partial \tilde{\gamma}_{ij}}{\partial t}. \tag{2.145}$$

In terms of shift vector we can express it as

$$Q_{ij} = -2NA_{ij} + (L\beta)_{ij}, \tag{2.146}$$

The minimal distortion means that

$$D^j Q_{ij} = 0. \tag{2.147}$$

Thus we have the equation for the shift

$$D_j D^j \beta^i + \frac{1}{3} D^i D_j \beta^j + R^i{}_j \beta^j = 16\pi N p^i + \frac{4}{3} N D^i K + 2A^{ij} D_j N. \tag{2.148}$$

On the other hand we may rewrite Eq. (2.145) as

$$Q_{ij} = \frac{\partial \gamma_{ij}}{\partial t} - 4\frac{\partial}{\partial t}\ln\Psi\,\gamma_{ij} = \Psi^4 \frac{\partial \tilde{\gamma}_{ij}}{\partial t}. \tag{2.149}$$

The minimal distortion condition can be expressed in terms of the time derivative of the conformal metric by combining Eqs. (2.145) and (2.147):

$$D^j(\Psi^4 \dot{\tilde{\gamma}}_{ij}) = 0. \tag{2.150}$$

or

$$\tilde{D}^j(\Psi^6 \dot{\tilde{\gamma}}_{ij}) = 0. \tag{2.151}$$

The drawback of the coordinate choice is that it is expensive to implement.

### 2.5.3 Approximate minimal distortion

In view of Eq. (2.151), it is natural to consider the simpler condition

$$\tilde{D}^j \dot{\tilde{\gamma}}_{ij} = 0, \tag{2.152}$$

Since

$$\dot{\tilde{\gamma}}_{ij} = -2N\tilde{A}_{ij} + \tilde{\gamma}_{ik}\tilde{\gamma}_{jl}(\tilde{L}\beta)^{kl}. \tag{2.153}$$

Equation (2.152) becomes then

$$\tilde{D}^j \left[\tilde{\gamma}_{ik}\tilde{\gamma}_{jl}(\tilde{L}\beta)^{kl} - 2N\tilde{A}_{ij}\right] = 0, \tag{2.154}$$

or

$$\tilde{D}_j\tilde{D}^j\beta^i + \frac{1}{3}\tilde{D}^i\tilde{D}_j\beta^j + \tilde{R}^i{}_j\beta^j - 2\tilde{A}^{ij}\tilde{D}_j N + 4N\left[3\tilde{A}^{ij}\tilde{D}_j\ln\Psi - \frac{1}{3}\tilde{D}^i K - 4\pi\Psi^4 p^i\right] = 0. \tag{2.155}$$

Replace the connection associated with metric $\tilde{\gamma}$ by the one with flat metric $\mathbf{f}$, we have instead of Eq. (2.152)

$$\mathcal{D}^j \dot{\tilde{\gamma}}_{ij} = 0, \tag{2.156}$$

or the equation for $\beta$

$$\mathcal{D}_j \mathcal{D}^j \beta^i + \frac{1}{3}\mathcal{D}^i \mathcal{D}_j \beta^j - 2\tilde{A}^{ij}\tilde{D}_j N + 4N\left[3\tilde{A}^{ij}\tilde{D}_j \ln\Psi - \frac{1}{3}\tilde{D}^i K - 4\pi\Psi^4 p^i\right] = 0. \tag{2.157}$$

This is called **approximate minimal distortion**.

### 2.5.4 Gamma freezing

Define

$$\tilde{\Gamma}^i := \tilde{\gamma}^{jk}\left(\tilde{\Gamma}^i{}_{jk} - \bar{\Gamma}^i{}_{jk}\right) = -\mathcal{D}_j \tilde{\gamma}^{ij}, \tag{2.158}$$

then the Gamma freezing condition is set to

$$\frac{\partial \tilde{\Gamma}^i}{\partial t} = -\frac{\partial}{\partial t}\left(\mathcal{D}_j \tilde{\gamma}^{ij}\right) = -\mathcal{D}_j \dot{\tilde{\gamma}}^{ij} = 0, \tag{2.159}$$

This is equivalent to

$$\begin{aligned}\tilde{\gamma}^{jk}\mathcal{D}_j\mathcal{D}_k\beta^i + \frac{1}{3}\tilde{\gamma}^{ij}\mathcal{D}_j\mathcal{D}_k\beta^k + \frac{2}{3}\tilde{\Gamma}^i\mathcal{D}_k\beta^k - \tilde{\Gamma}^k\mathcal{D}_k\beta^i + \beta^k\mathcal{D}_k\tilde{\Gamma}^i = \\ 2N\left[8\pi\Psi^4 p^i - \tilde{A}^{jk}\left(\tilde{\Gamma}^i{}_{jk} - \bar{\Gamma}^i{}_{jk}\right) - 6\tilde{A}^{ij}\mathcal{D}_j \ln\Psi + \frac{2}{3}\tilde{\gamma}^{ij}\mathcal{D}_j K\right] + 2\tilde{A}^{ij}\mathcal{D}_j N.\end{aligned} \tag{2.160}$$

The advantage of using this is that it provides similar stability as the minimal distortion coordinates, while being simple to implement. This is the spatial coordinate condition we use most commonly in our numerical simulations.

## 2.6 Schemes for evolution

Even after having selected the foliation and the spatial coordinates propagation (Sec. 2.4), there remains different strategies to integrate the 3+1 Einstein equations, either in their original form (2.78)-(2.81), or in the conformal form (2.128)-(2.133). In particular, the constraint equations (2.80)-(2.81) or (2.132)-(2.133) may be solved or not during the evolution, giving rise to respectively the so-called *free evolution schemes* and the *constrained schemes*.

### 2.6.1 Constrained schemes

A ***constrained scheme*** is a time scheme for integrating the 3+1 Einstein system in which some (***partially constrained scheme***) or all (***fully constrained scheme***) of the four constraints are used to compute some of the metric coefficients at each step of the numerical evolution.

### 2.6.2 Free evolution schemes

We can derive from the Einstein equations that

$$\left(\frac{\partial}{\partial t} - \mathcal{L}_\beta\right) H = -D_i(NM^i) + 2NKH - M^i D_i N \tag{2.161}$$

$$\left(\frac{\partial}{\partial t} - \mathcal{L}_\beta\right) M^i = -D^i(NH) + 2NK^i{}_j M^j + NKM^i + HD^i N. \tag{2.162}$$

here $\mathbf{H}, \mathbf{M^i}$ are the Hamiltonian, momentum constraints, respectively. If the constraints are satisfied at $t = 0$, i.e., $H|_{t=0} = 0$ and $M^i|_{t=0} = 0$, then

$$\forall t \geq 0, \quad H = 0 \quad \text{and} \quad M^i = 0, \tag{2.163}$$

i.e. the constraints are preserved by the time evolution. This means that we can solve the equations without make use of the constraints equations. In this scheme we need to assume that the violation from numerical errors and error from the boundary conditions remain small throughout the evolution. The constraints can then be used to monitor the accuracy of the numerical evolution. We use this strategy in all of our numerical studies.

### 2.6.3 Evolution scheme of our study

In this thesis we based our study on the conformal 3+1 Einstein equations with a particular choice of variables first proposed by Ref. [12, 13, 14].

One can define

$$\Delta^k{}_{ij} := \tilde{\Gamma}^k{}_{ij} - \bar{\Gamma}^k{}_{ij} = \frac{1}{2}\tilde{\gamma}^{kl}\left(\mathcal{D}_i\tilde{\gamma}_{lj} + \mathcal{D}_j\tilde{\gamma}_{il} - \mathcal{D}_l\tilde{\gamma}_{ij}\right), \tag{2.164}$$

with

$$\Delta^k{}_{ik} = \frac{1}{2}\frac{\partial}{\partial x^i}\ln\tilde{\gamma} - \frac{1}{2}\frac{\partial}{\partial x^i}\ln f = 0. \tag{2.165}$$

We can express the Ricci tensor as

$$\begin{aligned}\tilde{R}_{ij} &= \frac{\partial}{\partial x^k}\tilde{\Gamma}^k{}_{ij} - \frac{\partial}{\partial x^j}\tilde{\Gamma}^k{}_{ik} + \tilde{\Gamma}^k{}_{ij}\tilde{\Gamma}^l{}_{kl} - \tilde{\Gamma}^k{}_{il}\tilde{\Gamma}^l{}_{kj} \\ &= \frac{1}{2}\left(-\tilde{\gamma}^{kl}\mathcal{D}_k\mathcal{D}_l\tilde{\gamma}_{ij} + \tilde{\gamma}_{ik}\mathcal{D}_j\tilde{\Gamma}^k + \tilde{\gamma}_{jk}\mathcal{D}_i\tilde{\Gamma}^k\right) + \mathcal{Q}_{ij}(\tilde{\gamma}, \mathcal{D}\tilde{\gamma}),\end{aligned} \tag{2.166}$$

and the Ricci scalar

$$\tilde{R} = \mathcal{D}_k \tilde{\Gamma}^k + \mathcal{Q}(\tilde{\gamma}, \mathcal{D}\tilde{\gamma}), \tag{2.167}$$

where

$$\mathcal{Q}(\tilde{\gamma}, \mathcal{D}\tilde{\gamma}) := \frac{1}{2}\tilde{\gamma}^{kl}\mathcal{D}_k\tilde{\gamma}^{ij}\,\mathcal{D}_l\tilde{\gamma}_{ij} + \tilde{\gamma}^{ij}\mathcal{Q}_{ij}(\tilde{\gamma}, \mathcal{D}\tilde{\gamma}), \tag{2.168}$$

and

$$\mathcal{Q}_{ij}(\tilde{\gamma}, \mathcal{D}\tilde{\gamma}) := -\frac{1}{2}\left(\mathcal{D}_k\tilde{\gamma}_{lj}\,\mathcal{D}_i\tilde{\gamma}^{kl} + \mathcal{D}_k\tilde{\gamma}_{il}\,\mathcal{D}_j\tilde{\gamma}^{kl} + \mathcal{D}_k\tilde{\gamma}^{kl}\,\mathcal{D}_l\tilde{\gamma}_{ij}\right) - \Delta^k{}_{il}\Delta^l{}_{kj}. \tag{2.169}$$

Then we can write the complete system of equations as:

$$\left(\frac{\partial}{\partial t} - \mathcal{L}_\beta\right)\Psi = \frac{\Psi}{6}\left(\tilde{D}_i\beta^i - NK\right), \tag{2.170}$$

$$\left(\frac{\partial}{\partial t} - \mathcal{L}_\beta\right)\tilde{\gamma}_{ij} = -2N\tilde{A}_{ij} - \frac{2}{3}\tilde{D}_k\beta^k\,\tilde{\gamma}_{ij}, \tag{2.171}$$

$$\left(\frac{\partial}{\partial t} - \mathcal{L}_\beta\right)K = -\Psi^{-4}\left(\tilde{D}_i\tilde{D}^iN + 2\tilde{D}_i\ln\Psi\,\tilde{D}^iN\right) + N\left[4\pi(E+S) + \tilde{A}_{ij}\tilde{A}^{ij} + \frac{K^2}{3}\right], \tag{2.172}$$

$$\begin{aligned}\left(\frac{\partial}{\partial t} - \mathcal{L}_\beta\right)\tilde{A}_{ij} \;=\; & -\frac{2}{3}\tilde{D}_k\beta^k\,\tilde{A}_{ij} + N\left[K\tilde{A}_{ij} - 2\tilde{\gamma}^{kl}\tilde{A}_{ik}\tilde{A}_{jl} - 8\pi\left(\Psi^{-4}S_{ij} - \frac{1}{3}S\tilde{\gamma}_{ij}\right)\right] \\ & +\Psi^{-4}\Big\{ -\tilde{D}_i\tilde{D}_jN + 2\tilde{D}_i\ln\Psi\,\tilde{D}_jN + 2\tilde{D}_j\ln\Psi\,\tilde{D}_iN \\ & \quad +\frac{1}{3}\left(\tilde{D}_k\tilde{D}^kN - 4\tilde{D}_k\ln\Psi\,\tilde{D}^kN\right)\tilde{\gamma}_{ij} \\ & \quad +N\Big[\frac{1}{2}\left(-\tilde{\gamma}^{kl}\mathcal{D}_k\mathcal{D}_l\tilde{\gamma}_{ij} + \tilde{\gamma}_{ik}\mathcal{D}_j\tilde{\Gamma}^k + \tilde{\gamma}_{jk}\mathcal{D}_i\tilde{\Gamma}^k\right) + \mathcal{Q}_{ij}(\tilde{\gamma}, \mathcal{D}\tilde{\gamma}) \\ & \quad -\frac{1}{3}\left(\mathcal{D}_k\tilde{\Gamma}^k + \mathcal{Q}(\tilde{\gamma}, \mathcal{D}\tilde{\gamma})\right)\tilde{\gamma}_{ij} - 2\tilde{D}_i\tilde{D}_j\ln\Psi + 4\tilde{D}_i\ln\Psi\,\tilde{D}_j\ln\Psi \\ & \quad\quad +\frac{2}{3}\left(\tilde{D}_k\tilde{D}^k\ln\Psi - 2\tilde{D}_k\ln\Psi\,\tilde{D}^k\ln\Psi\right)\tilde{\gamma}_{ij}\Big]\Big\},\end{aligned} \tag{2.173}$$

$$\begin{aligned}\left(\frac{\partial}{\partial t} - \mathcal{L}_\beta\right)\tilde{\Gamma}^i \;=\; & \frac{2}{3}\mathcal{D}_k\beta^k\,\tilde{\Gamma}^i + \tilde{\gamma}^{jk}\mathcal{D}_j\mathcal{D}_k\beta^i + \frac{1}{3}\tilde{\gamma}^{ij}\mathcal{D}_j\mathcal{D}_k\beta^k - 2\tilde{A}^{ij}\mathcal{D}_jN \\ & -2N\left[8\pi\Psi^4p^i - \tilde{A}^{jk}\Delta^i{}_{jk} - 6\tilde{A}^{ij}\mathcal{D}_j\ln\Psi + \frac{2}{3}\tilde{\gamma}^{ij}\mathcal{D}_jK\right]\end{aligned}, \tag{2.174}$$

where $\mathcal{Q}_{ij}(\tilde{\gamma}, \mathcal{D}\tilde{\gamma})$ and $\mathcal{Q}(\tilde{\gamma}, \mathcal{D}\tilde{\gamma})$ are defined by Eqs. (2.169) and (2.168).

$$\tilde{D}_i\tilde{D}^i\Psi - \frac{1}{8}\tilde{R}\Psi + \left(\frac{1}{8}\tilde{A}_{ij}\tilde{A}^{ij} - \frac{1}{12}K^2 + 2\pi E\right)\Psi^5 = 0, \tag{2.175}$$

$$\tilde{D}^j\tilde{A}_{ij} + 6\tilde{A}_{ij}\tilde{D}^j \ln\Psi - \frac{2}{3}\tilde{D}_i K = 8\pi p_i, \tag{2.176}$$

$$\det(\tilde{\gamma}_{ij}) = f, \tag{2.177}$$

$$\tilde{\gamma}^{ij}\tilde{A}_{ij} = 0, \tag{2.178}$$

$$\tilde{\Gamma}^i + \mathcal{D}_j\tilde{\gamma}^{ij} = 0. \tag{2.179}$$

This is the full set of the Einstein equations used in our numerical code. Next we go for the equations of hydrodynamic variables in a form suitable for evolution together with Eqs. (2.170)-(2.174).

Note that the 4-velocity $u_\mu$ is normalized $u^\mu u_\mu = -1$, so that its components can be written in terms of the three spatial velocity components $v^i$ as

$$\{u^\mu\} = \frac{W}{\alpha}\{1, \alpha v^i - \beta^i\}, \tag{2.180}$$

where $W$, instead of $\Gamma$ in Eq. (2.85), is the Lorentz factor $W = 1/\sqrt{1 - \gamma_{ij}v^iv^j}$, and $\alpha = \mathrm{N}$, is the lapse function (see Eq. (2.3)). The specific enthalpy, $h$, is given as

$$h = 1 + \epsilon + P/\rho, \tag{2.181}$$

where $\epsilon$ is the specific internal energy density.

The general relativistic hydrodynamics equations, which include the baryon number conservation of matter, Eq. (2.82), and the conservation equations of the energy momentum Eq. (2.89), can be written in first order, flux conservative form as

$$\partial_t\vec{\mathcal{U}} + \partial_i\vec{F}^i = \vec{S}, \tag{2.182}$$

where the conservative hydrodynamical variables $\vec{\mathcal{U}}$ are written in terms of the primitive variables $\{\rho, v^i, \epsilon\}$ as

$$\vec{\mathcal{U}} = \begin{bmatrix} D \\ S_j \\ \tau \end{bmatrix} = \begin{bmatrix} \sqrt{\gamma} W \rho \\ \sqrt{\gamma} \rho h W^2 v_j \\ \sqrt{\gamma}(\rho h W^2 - P - W\rho) \end{bmatrix}. \tag{2.183}$$

The flux vector $\vec{F}^i$ can be written as

$$\vec{F}^i = \begin{bmatrix} \alpha \left(v^i - \beta^i/\alpha\right) D \\ \alpha \left((v^i - \beta^i/\alpha) S_j + \sqrt{\gamma} P \delta^i_j\right) \\ \alpha \left((v^i - \beta^i/\alpha)\tau + \sqrt{\gamma} v^i P\right) \end{bmatrix}, \tag{2.184}$$

and the source vector $\vec{S}$ can be written as

$$\vec{S} = \begin{bmatrix} 0 \\ \alpha \sqrt{\gamma} T^{\mu\nu} g_{\nu\sigma} \Gamma^{\sigma}{}_{\mu j} \\ \alpha \sqrt{\gamma} (T^{\mu t} \partial_\mu \alpha - \alpha T^{\mu\nu} \Gamma^{t}{}_{\mu\nu}) \end{bmatrix}. \tag{2.185}$$

Eqs. (2.182)-(2.185) is the full set of general relativistic hydrodynamic equations used in our code.

In the case of the Einstein field equations, we expect the dynamical degrees of freedom to remain smooth and continuous for a well-behaving coordinate system. On the other hand, for the relativistic hydrodynamical equations, we know that shocks (discontinuities) can easily form. Thus, the discretization method for the hydrodynamical equations must be able to handle accurately the propagation of shocks. The approach we use is based on the High Resolution Shock Capturing (HRSC) techniques

(see [15]). We use a Roe's approximate Riemann solver throughout the work on the critical phenomena [15].

For the coordinate conditions to go with the evolution equations (2.170)-(2.174) and (2.182)-(2.185), we implement a variant of the so-called "1+log" slicing condition for the lapse,

$$\frac{\partial \alpha}{\partial t} = -2\alpha K. \tag{2.186}$$

Note that this is a completely local condition, and is therefore computationally inexpensive.

For the conditions on the shift, we use a modification of the "Gamma-Freezing" shift equation [16]. Specifically, we implement the first integral form of the hyperbolic Gamma-driver (Eq. (46) of reference [16]),

$$\frac{\partial \beta^i}{\partial t} = C_1 \tilde{\Gamma}^i - C_2 \beta^i, \tag{2.187}$$

where we set the constants $C_1 = C_2 = 0.8$ for all numerical simulations in this thesis.

## 2.7 The construction of initial data

The initial data for the evolution must satisfy the Hamiltonian and momentum constraint equations (2.80)-(2.81) and in a form suitable for evolution with the system (2.170)-(2.174) and (2.182)-(2.185). Next we describe the construction of such initial data.

### 2.7.1 Conformal decomposition of the constraints

With the conformal metric Eq. (2.92) and the traceless part of the extrinsic curvature of the form:

$$A^{ij} = \Psi^{-10}\hat{A}^{ij}, \tag{2.188}$$

we can derive the constraints equations as:

$$\tilde{D}_i\tilde{D}^i\Psi - \frac{1}{8}\tilde{R}\Psi + \frac{1}{8}\hat{A}_{ij}\hat{A}^{ij}\,\Psi^{-7} + 2\pi\tilde{E}\Psi^{-3} - \frac{1}{12}K^2\Psi^5 = 0, \tag{2.189}$$

$$\tilde{D}_j\hat{A}^{ij} - \frac{2}{3}\Psi^6\tilde{D}^iK = 8\pi\tilde{p}^i, \tag{2.190}$$

where we have introduce the rescaled matter quantities

$$\tilde{E} := \Psi^8 E, \tag{2.191}$$

and

$$\tilde{p}^i := \Psi^{10}p^i. \tag{2.192}$$

### 2.7.2 Longitudinal/transverse decomposition of $\hat{A}^{ij}$

Decompose $\hat{A}^{ij}$ into a longitudinal part and a transverse one, by setting

$$\hat{A}^{ij} = (\tilde{L}X)^{ij} + \hat{A}^{ij}_{\mathrm{TT}}, \tag{2.193}$$

where $\hat{A}^{ij}_{\mathrm{TT}}$ is both traceless and transverse (i.e. divergence-free) with respect to the metric $\tilde{\gamma}$:

$$\tilde{\gamma}_{ij}\hat{A}^{ij}_{\mathrm{TT}} = 0 \qquad \text{and} \qquad \tilde{D}_j\hat{A}^{ij}_{\mathrm{TT}} = 0, \tag{2.194}$$

and $(\tilde{L}X)^{ij}$ is the **conformal Killing operator** associated with the metric $\tilde{\gamma}$ and acting on the vector field $\mathbf{X}$:

$$(\tilde{L}X)^{ij} := \tilde{D}^i X^j + \tilde{D}^j X^i - \frac{2}{3}\tilde{D}_k X^k \tilde{\gamma}^{ij}. \tag{2.195}$$

it is traceless

$$\tilde{\gamma}_{ij}(\tilde{L}X)^{ij} = 0, \tag{2.196}$$

and the kernel of $\tilde{\mathbf{L}}$ is made of the **conformal Killing vectors** of the metric $\tilde{\gamma}$, i.e. the generators of the conformal isometrics. The symmetric tensor $(\tilde{L}X)^{ij}$ is called the *longitudinal part* of $\hat{A}^{ij}$, whereas $\hat{A}^{ij}_{\mathrm{TT}}$ is called the *transverse part*.

Introducing the **conformal vector Laplacian $\tilde{\mathbf{\Delta}}_L$**:

$$\tilde{\Delta}_L X^i := \tilde{D}_j(\tilde{L}X)^{ij} = \tilde{D}_j\tilde{D}^j X^i + \frac{1}{3}\tilde{D}^i\tilde{D}_j X^j + \tilde{R}^i{}_j X^j, \tag{2.197}$$

then by taking the divergence of Eq. (2.193): taking into account property (2.194), we have

$$\tilde{\Delta}_L X^i = \tilde{D}_j(\tilde{L}X)^{ij} = \tilde{D}_j\hat{A}^{ij}. \tag{2.198}$$

### 2.7.3 Conformal transverse-traceless form of the constraints

Inserting the longitudinal/transverse decomposition (2.193) into the constraint equations (2.189) and (2.190) and making use of Eq. (2.198) yields to the system

$$\tilde{D}_i\tilde{D}^i\Psi - \frac{1}{8}\tilde{R}\Psi + \frac{1}{8}\left[(\tilde{L}X)_{ij} + \hat{A}^{\mathrm{TT}}_{ij}\right]\left[(\tilde{L}X)^{ij} + \hat{A}^{ij}_{\mathrm{TT}}\right]\Psi^{-7} + 2\pi\tilde{E}\Psi^{-3} - \frac{1}{12}K^2\Psi^5 = 0, \tag{2.199}$$

$$\tilde{\Delta}_L X^i - \frac{2}{3}\Psi^6\tilde{D}^i K = 8\pi\tilde{p}^i, \tag{2.200}$$

where

$$(\tilde{L}X)_{ij} := \tilde{\gamma}_{ik}\tilde{\gamma}_{jl}(\tilde{L}X)^{kl}, \tag{2.201}$$

$$\hat{A}^{\rm TT}_{ij} := \tilde{\gamma}_{ik}\tilde{\gamma}_{jl}\hat{A}^{kl}_{\rm TT}. \tag{2.202}$$

Then the strategy we use to get valid initial data for the Cauchy problem is to choose $(\tilde{\gamma}_{ij}, \hat{A}^{ij}_{\rm TT}, K, \tilde{E}, \tilde{p}^i)$ on $\Sigma_0$ and solve the system (2.199)-(2.200) to get $\Psi$ and $X^i$. Then one constructs

$$\gamma_{ij} = \Psi^4\tilde{\gamma}_{ij}, \tag{2.203}$$

$$K^{ij} = \Psi^{-10}\left((\tilde{L}X)^{ij} + \hat{A}^{ij}_{\rm TT}\right) + \frac{1}{3}\Psi^{-4}K\tilde{\gamma}^{ij}, \tag{2.204}$$

$$E = \Psi^{-8}\tilde{E}, \tag{2.205}$$

$$p^i = \Psi^{-10}\tilde{p}^i, \tag{2.206}$$

and obtains a set $(\gamma, \mathbf{K}, E, \mathbf{p})$ which satisfies the constraint equations (2.80)-(2.81).

# Chapter 3

# The GRAstro-2D code

In this chapter we describe our effort to construct a code for solving the Einstein system derived in the previous chapter. We take the simplifying assumption of axisymmetry in order to achieve the resolution needed for the critical collapse study. Even under the axisymmetry assumption, the numerical calculation can only be carried out using massively parallel computers at the national supercomputing centers.

## 3.1 Realizing axisymmetry in a 3D Cartesian system

For an axisymmetric system the most natural coordinates are cylindrical $(\rho, z, \phi)$ or spherical $(r, \theta, \phi)$ coordinates. In such polar coordinates, we can ignore one spatial dimension(say, $(\phi)$), and apply boundary conditions easily.

However in the polar coordinates, there is a severe instability problem near the

axis ($\rho = 0$, or $\theta = 0$). One can easily see that there exits many singular terms in some Ricci tensor elements for $\theta \to 0$. Though these terms will cancel each other and give finite results when we do analytical calculations, the numerical errors will, when divided by terms that vanish at the axis, lead to instability. One may want to use the "numerical regularization" method of Evans [17], by redefining the improper variables, but this has only limited success. If limited to a diagonal 3-metric [18], one can get a long time stability, with the additional cost of solving several additional linear elliptic partial differential equations. So this treatment cannot save much computational time. Also, due to the logarithm coordinate, lots of computational efforts would be wasted inside the horizon when there is one, while extra computational effort would be needed to accurately represent gravitational wave outside.

Instead of going to a $(r, \theta, \phi)$ coordinate, we employed an idea first developed in Ref. [19] to handle axisymmetric simulations of vacuum spacetime. It solves only one single 2D slice (i.e. the $y = 0$ $x - z$ plane) of the 3D Cartesian grid, then rotate this slice about the $z$ axis to get the solution at any other (the $y \neq 0$) slices to calculate the derivatives of $y-$direction in the 3D code. We can call this quasi-2D grid. Through this we can have the singularity-free property of the 3D Cartesian coordinates, while reducing the computer memory and time usage at the same time.

We extended the quasi-2D grid treatment to non-vacuum spacetime, and in particular, for the solving of the general relativistic hydrodynamic equations. Based on our 3D Cartesian general-relativistic hydrodynamics code GRAstro [20] (Ref. [15, 21] presented the formulations and tested the consistency and convergence of GRAstro

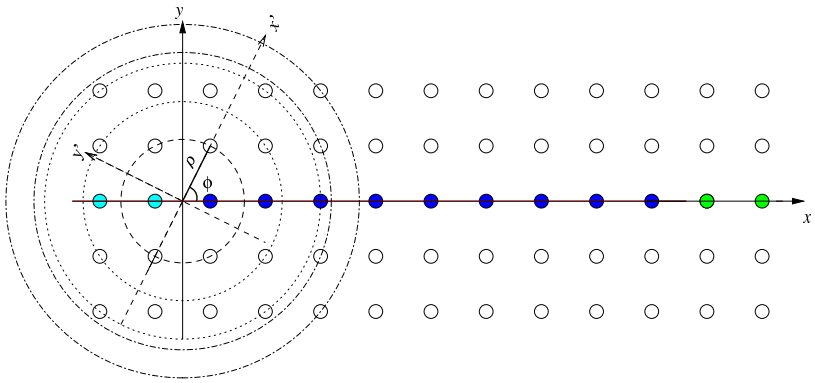


Figure 3.1: Our grid in a constant $z$ plane with $\Delta x = \Delta y$, staggering in x and z, not y, with a stencil size 2. The dashed, dotted, dash-dotted circles show the rotation about z axis, the solid circles represent grid points. The full filled ones are those we actually evaluate using the standard 3D finite difference code, the partly filled ones are obtained by the boundary condition after the evolution. The open ones represent stencil points which are needed for calculating of space derivations and can be obtained by interpolation and symmetry transformation discussed above.

code), we introduce the quasi-2D grid technique and the development of GRAstro-2D in Sec. 3.2. In Sec. 3.3, we present testings of GRAstro-2D with a single static neutron star with spherical symmetry (so-called TOV [10] star), a boosted TOV star [15], and two TOV stars in head-on collisions.

## 3.2 The construction of the GRAstro-2D code

For a system axisymmetric about the z-axis, the most economical treatment is to evolve only one radial slice. We applied the same 3D updating method to solve the equations for points along x-axis (y=0 plane), shown as filled solid circles in Fig. 3.1, and then, use 3D boundary conditions to get the values on the half-filled points. Thus

we get fields on the full $y = 0$ slice at each time step. To get values on stencil points (open solid circles), we make use of the axisymmetry and do interpolations.

By axisymmetry, every component of a tensor should be exactly the same for all points on a dash-dotted circle. That is,

$$T^{i'_1,i'_2,\cdots}_{j'_1,j'_2,\cdots}(x',0,z') = T^{i_1,i_2,\cdots}_{j_1,j_2,\cdots}(\rho,0,z). \tag{3.1}$$

with $\rho = x' = \sqrt{(}x^2+y^2)$, $z = z'$, and $i'_s = i_s$, ... , $j'_s = j_s$, ... , representing two sets of indices in different coordinates $(x', y', z')$ and $(x, y, z)$, respectively. Since the calculation is running on $(x, y, z)$ coordinates, we need a transformation from $(x', y', z')$ to $(x, y, z)$ for any grid point:

$$\left(\frac{\partial x^i}{\partial x'^j}\right) = \begin{pmatrix} \cos\phi & -\sin\phi & 0 \\ \sin\phi & \cos\phi & 0 \\ 0 & 0 & 1 \end{pmatrix}, \left(\frac{\partial x'^i}{\partial x^j}\right)(\phi) = \left(\frac{\partial x^i}{\partial x'^j}\right)(-\phi). \tag{3.2}$$

Thus the components of a tensor at point $(x, y, z)$ are

$$T^{i_1,i_2,\cdots}_{j_1,j_2,\cdots}(x,y,z) = \left(\frac{\partial x^{i_1}}{\partial x'^{i_1}}\right)\left(\frac{\partial x^{i_2}}{\partial x'^{i_2}}\right)\cdots\left(\frac{\partial x'^{j_1}}{\partial x^{j_1}}\right)\left(\frac{\partial x'^{j_2}}{\partial x^{j_2}}\right)\cdots T^{i'_1,i'_2,\cdots}_{j'_1,j'_2,\cdots}(x',0,z'), \tag{3.3}$$

By the symmetry condition Eq. (3.1) we get

$$T^{i_1,i_2,\cdots}_{j_1,j_2,\cdots}(x,y,z) = \left(\frac{\partial x^{i_1}}{\partial x'^{k_1}}\right)\left(\frac{\partial x^{i_2}}{\partial x'^{k_2}}\right)\cdots\left(\frac{\partial x'^{l_1}}{\partial x^{j_1}}\right)\left(\frac{\partial x'^{l_2}}{\partial x^{j_2}}\right)\cdots T^{k_1,k_2,\cdots}_{l_1,l_2,\cdots}(\sqrt{x^2+y^2},0,z). \tag{3.4}$$

This equation describes how to compute the components of a tensor in the stencil grid points within the half-plane $x \geq 0$ from corresponding points on $y = 0$ slice in

Fig. 3.1. Next we need to connect points on $y = 0$ slice to the filled circles (calculated grid points). This can be done by polynomial interpolations. We find that, except for the outer boundary points, 4th order polynomials give good results.

## 3.3 Convergence test

A solution of Einstein equations should satisfy the Hamiltonian and momentum constraints. In numerical simulation, the error **e** due to finite differencing should decrease to zero with reduced step length h (i.e., higher resolution).

Our code is convergent to second order ( the error $e \propto h^2$) at time t=0 for the solving of the initial constraint equations, and first order ($e \propto h$) for the evolution equations due to the use of the high resolution shock capturing(HRSC) scheme with flux limiters (see refs. [22, 23, 15]). To show the convergence in a figure, we scale the constraint violations at time t (corresponding to different resolutions) so that they should overlap: for solution 1 with step length $h_1$, error $e_1$, solution 2 with $h_2 = (1/2)h_1$, error $e_2$, then we should have $e_2 = (1/2)e_1$ if the solution is first order convergent ($2e_2$ will overlap with $e_1$, we call $2e_2$ as scaled $e_2$ in a fig.), or $e_2 = (1/4)e_1$ if it is second order convergent ($4e_2$ will overlap with $e_1$).

### 3.3.1 Convergence over resolution

The numerical solutions should be convergent when the resolution is raised (the step length $h \rightarrow 0$). Fig. 3.2 and 3.3 show the convergence of Hamiltonian constraint with 6 different resolutions that goes as high as to h=0.01 for the evolution of a static TOV star [10] and boosted TOV star [15] initial data, respectively. The boosted TOV test is a particularly useful test as it is a test bed that has an analytic solution and at the same time involves all terms in the coupled Einstein and general relativistic hydrodynamic system. For t=0, they showed the 2nd order convergence behavior. For a later time they showed a convergence that's higher than the first order but lower than 2nd order, i.e., the separation between the solution curve with highest resolution and the one with second highest is smaller than the one between the curve with 2nd highest and the one with the 3rd highest, etc., which is expected convergence behavior. Fig. 3.4 shows the convergence of the Hamiltonian constraint error for head-on collision of two neutron stars with 3 resolutions and at various times. That the convergence properties are correct throughout the time of evolution is one of the most important validation of a numerical code.

### 3.3.2 Convergence over boundary size

To show the effect of the size of computational domain on the simulation, we plot the convergence of the momentum constraints over time (Fig. 3.5). Because of the reflection from the outer boundary of the computational domain, which is 62 $M_{\odot}$ in

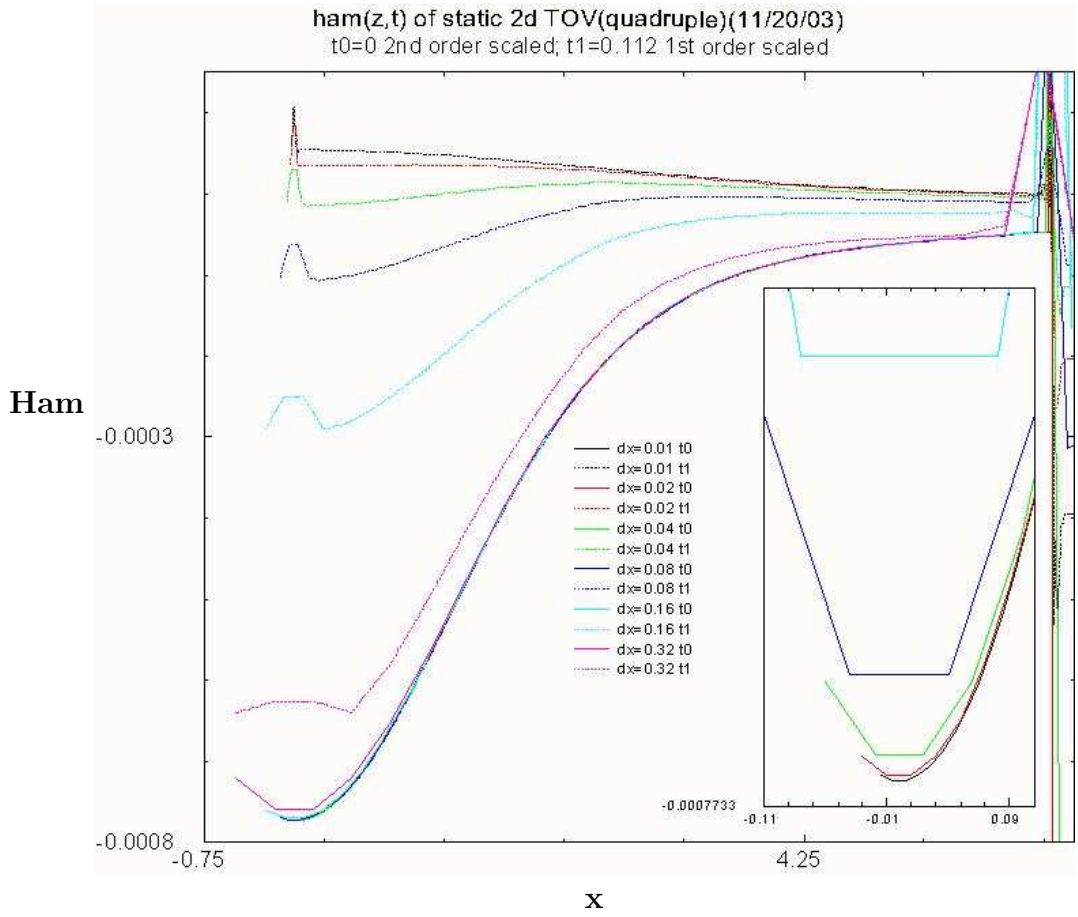


Figure 3.2: Hamiltonian constraint distribution for static TOV star in 6 different resolutions. All curves of t=0 overlapped with each other after scaling. More details are shown in the right lower box.

this study, the convergence is ruined at the outer region. Fig. 3.6 shows that the amplitude of momentum constraints is reduced when we increase the boundary size. Fig. 3.7 shows the effect of the domain size on the convergence of the Hamiltonian constraint. All curves in the figure overlap, although they correspond to different boundary sizes.

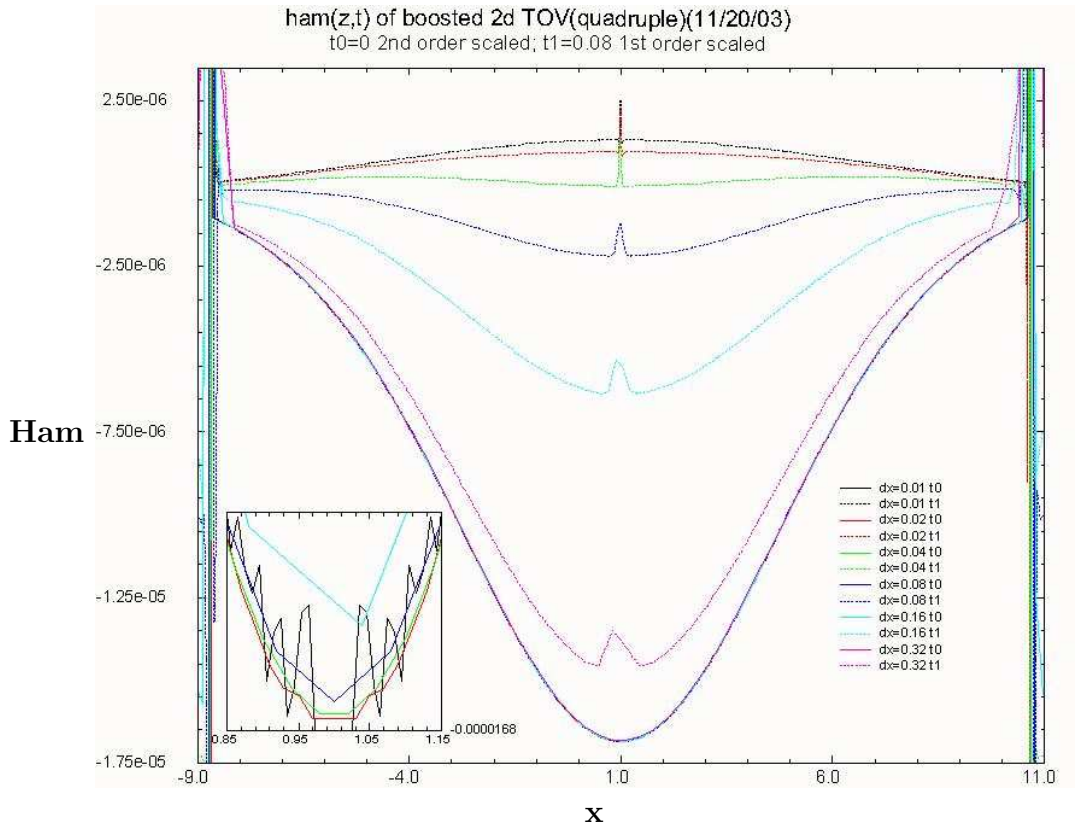


Figure 3.3: Hamiltonian constraint distribution for boosted TOV star in 6 different resolutions. All curves of t=0 overlapped with each other after scaling. They are enlarged to show details in the left lower box.

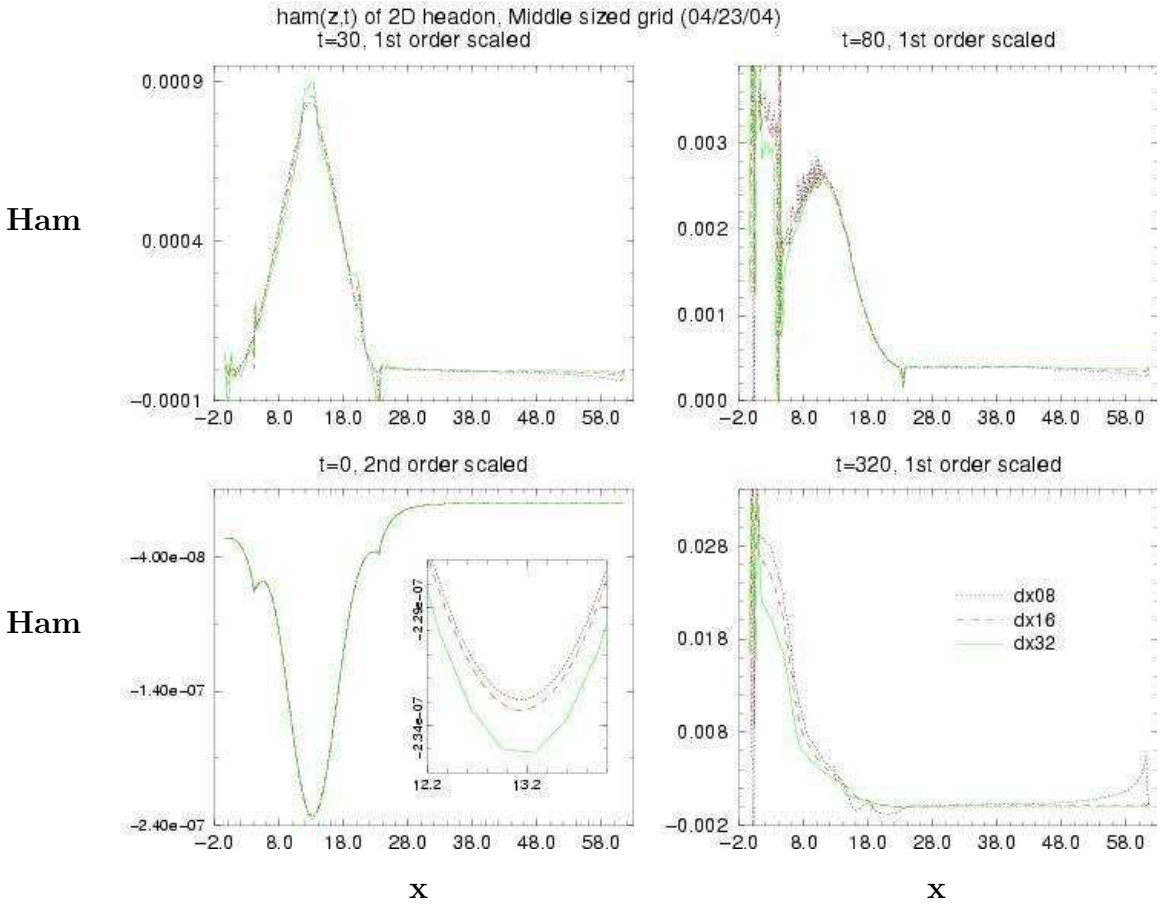


Figure 3.4: Hamiltonian constraint distribution for head-on collision of Neutron stars at 4 different time.

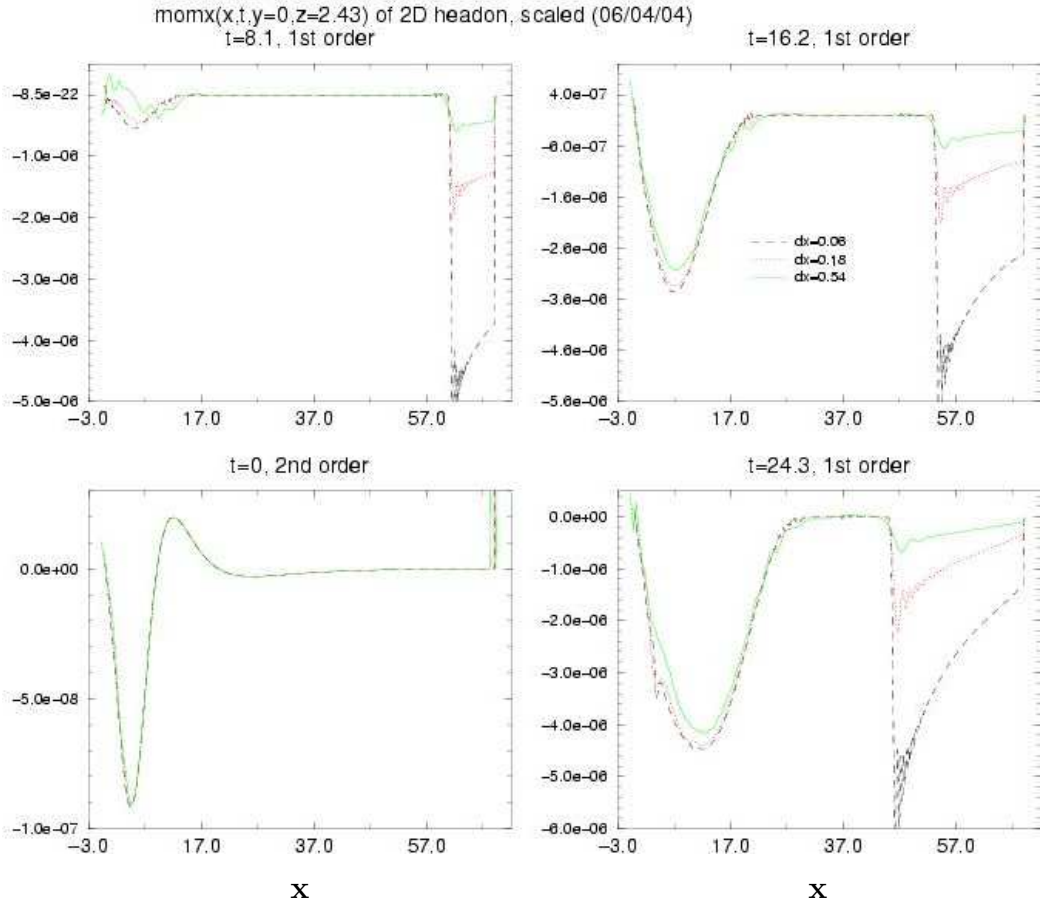


Figure 3.5: Momentum constraint distribution for head-on collision of Neutron stars at 4 different time.

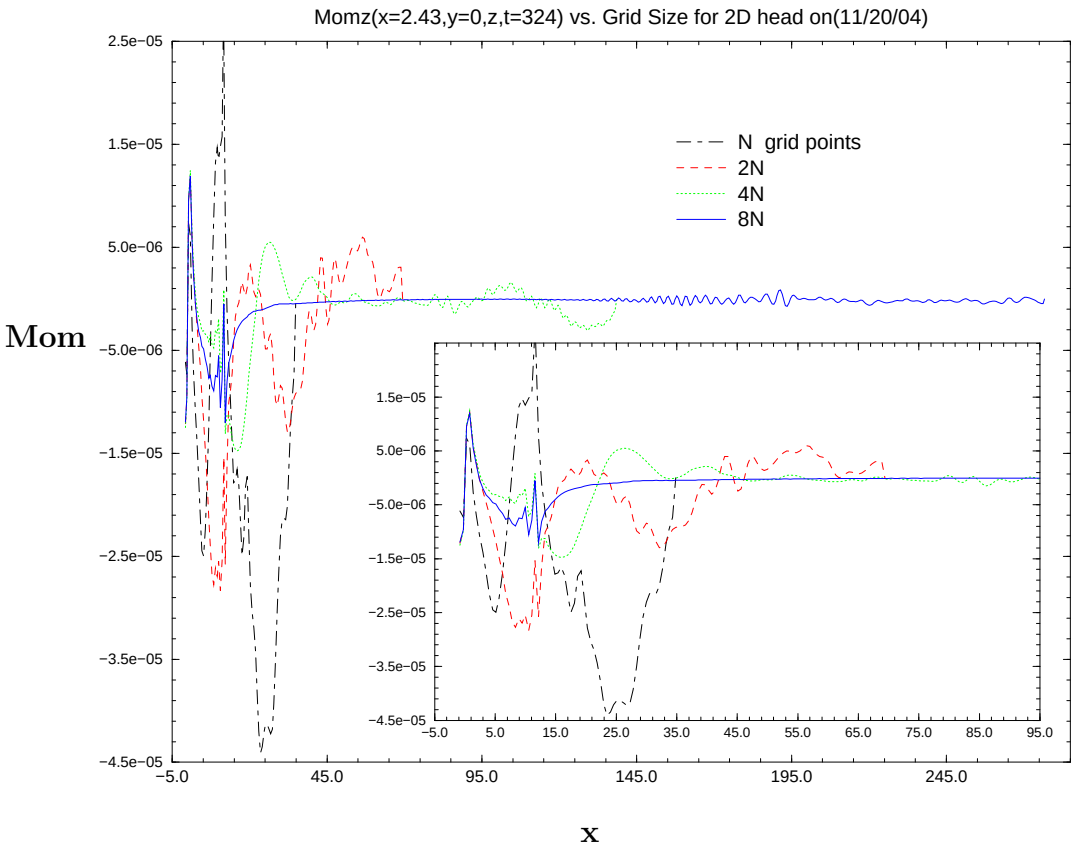


Figure 3.6: Momentum constraint distribution for head-on collision of Neutron stars in 4 different grid sizes (4 curves end in different boundaries). The small box shows the constraint curves in more detail in a grid size $2N$, half of the bigger one. The momentum constraint decreases with increased grid size.

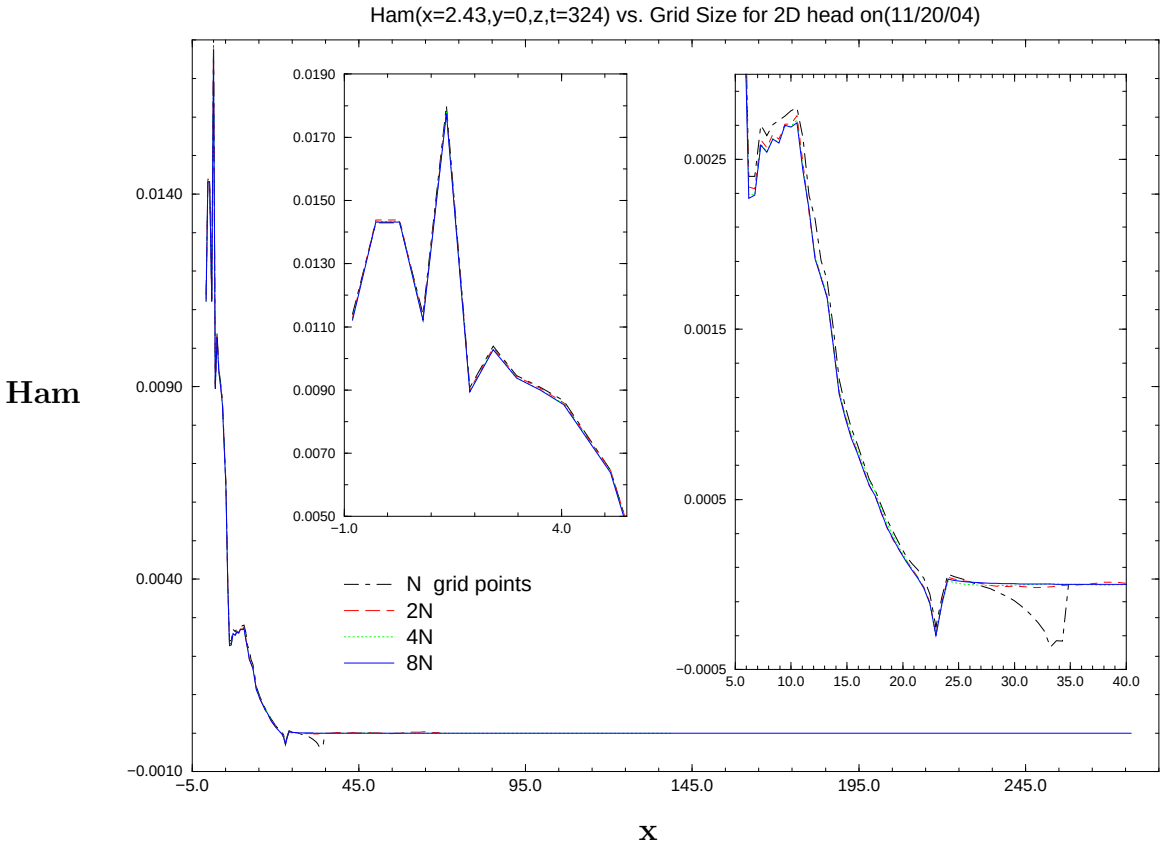


Figure 3.7: Hamiltonian constraint distribution for head-on collision of Neutron stars in 4 different grid sizes. There are 3 boxes in the fig. The smallest, the medium and the largest one shows the ham in the central, a region corresponds to the grid size $N$ and $4N$, respectively. It shows that the Hamiltonian constraint is not affected by increasing the grid size.

# Chapter 4

# The critical gravitational collapse of a non-rotating neutron star system

## 4.1 Initial configuration

We use the polytropic equation of state (EOS): $P = (\Gamma - 1)\rho\epsilon$ with $\Gamma = 2$ (and cases close to 2). Here $\rho$ is the proper rest mass density and $\epsilon$ is the proper specific internal energy density. Notice that the "kinetic-energy-dominated" assumption has not been made, unlike earlier investigations of the critical collapses of perfect fluid systems (for review, see [24, 3, 2]). Initial data sets are constructed with $P = k\rho^{\Gamma}$, where $k = 0.0298c^2/\rho_n$ ($\rho_n$ is the nuclear density, approximately 2.3 x $10^{14}$ g/cm$^3$). For this EOS, the maximum stable neutron star (NS) configuration has an Arnowitt-

Deser-Misner (ADM) mass of $1.46M_{\odot}$ and a baryonic mass of $1.61M_{\odot}$.

To save computer memory and time, we put two TOV stars symmetrically about $z = 0$ surface centered on the z axis so that we can use octant symmetry with the simulations. The TOV stars are boosted in same speed but in opposite direction to collide head-on.

## 4.2 Type I Critical Phenomena

The type I critical phenomena have been found on the critical surface dividing the black holes and stars with exotic EOS (see reviews [3, 4]). It is found on the surface that the black hole formed has a finite mass. The solutions near the critical solution takes the following form

$$Z(\mathbf{x}, t) \simeq Z_*(\mathbf{x}) + \frac{dC_0}{dp}(p_*)(p - p_*)e^{\lambda_0 t}Z_0(\mathbf{x}) + decaying\ modes \tag{4.1}$$

so we have the life-time of a solution that is close to the critical one given by

$$t_p = -\lambda_0^{-1} ln|p - p_*| + const \tag{4.2}$$

## 4.3 Existence of the Critical Phenomena in Head-on Collisions of NSs of non-exotic matter.

In the first set of simulations, the two NSs are initially at a fixed distance (the maximum density points of the two NSs are separated by $3R$, where $R \sim 9.1M_{\odot}$ is

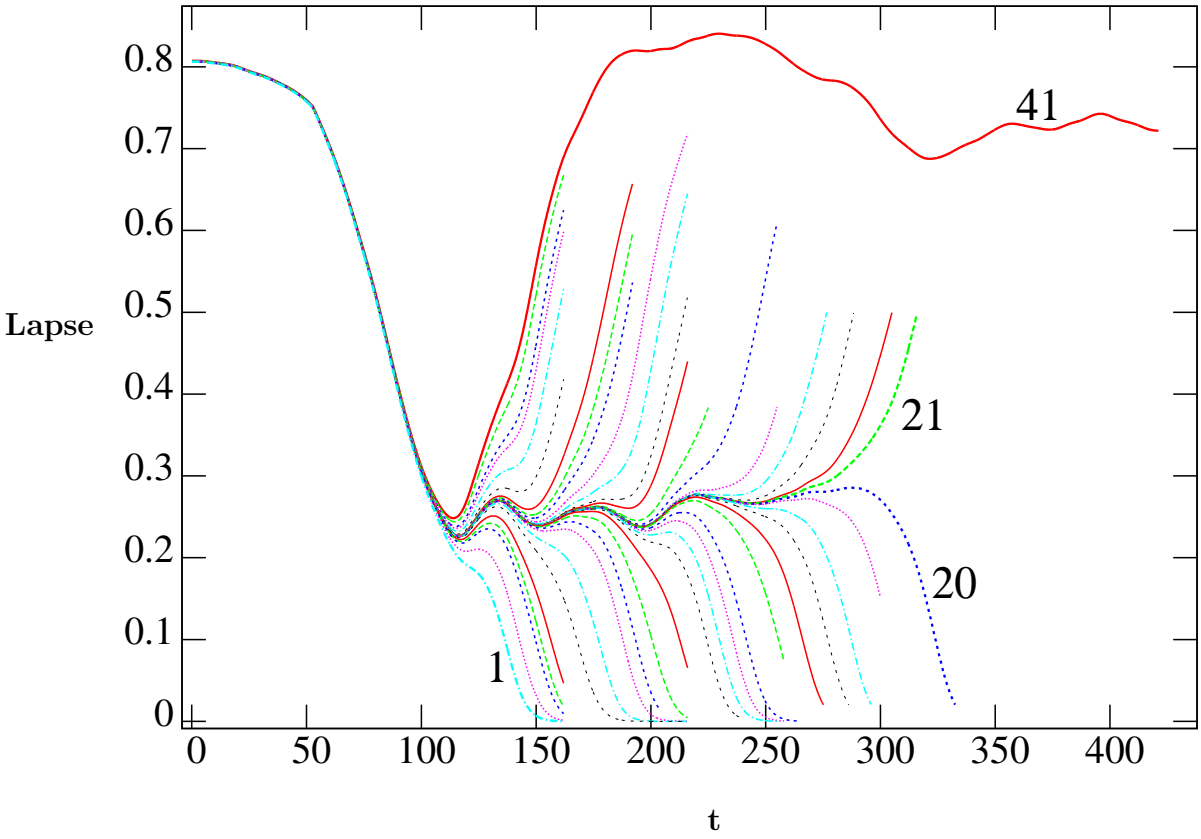


Figure 4.1: Lapse functions at the center of collision vs. time for NSs with slightly different masses, for the case of dx=0.12.

the coordinate radius of the NSs). The initial velocities of the NSs are that of freely falling from infinity, determined by the Newtonian formula plus the 1PN (first order Post-Newtonian) correction [10]. For example when the baryonic mass of each of the NS is in the range of $0.786M_\odot$ to $0.793M_\odot$, the initial speed ranges from 0.15537 to 0.15584 (in units of $c = 1$). The computational grid has $323 \times 5 \times 323$ points, covering a computational domain of $(\pi r^2 \times \text{height}\ ) = (\pi \times 38.5^2 \times 77.0){M_\odot}^3$. Each NS radius is resolved with 76 grid points, taking advantage of the octane- and axi-symmetry of the problem.

Fig. 4.1 shows the evolution of the lapse function $\alpha$ at the center of the collision as a function of the coordinate time, for systems with slightly different masses (all other parameters, including physical and numerical parameters, are the same). The line labeled 1 in Fig. 4.1 (which dips to 0 near $t \sim 150M_{\odot}$) represents the case of $0.793M_{\odot}$. We see that after the collision, $\alpha$ promptly "collapses" to zero, signaling the formation of a black hole. Note that the total baryonic mass of the merged object $1.59M_{\odot}$ is *less* than the maximum stable mass of a TOV solution of the same EOS in equilibrium. The prompt gravitational collapse of the merged object with such a mass indicates that it is in a state that is very different from being stationary [21, 25].

The line labeled 41 in Fig. 4.1 (which rises at $t \sim 120M_{\odot}$) represents the case where each of the NSs has the baryonic mass $0.786M_{\odot}$. The lapse at the collision center dips as the two stars merge, then rebounds. The merged object does not collapse to a black hole but instead form a stable NS in axisymmetric oscillations. The lapse at the center of the merged object oscillates around a value of 0.71, with a period of about $160M_{\odot}$.

For configurations with masses between the bottom line (1) and top line (41), the lapse $\alpha$ would rebound, dip etc., before eventually dipping to zero (a black hole is formed) or going back up (a NS is formed). The critical solution is found by fine tuning $\rho_c$, the proper mass density as measured by an observer at rest with the fluid at the center of the star at the initial time. For the numerical setup used in the study, at around $\rho_c = 6.128202618199 \times 10^{-4}$ (mass of each NS $= 0.79070949026M_{\odot}$), a change of the $\rho_c$ by the $10^{th}$ significant digit changes the dynamics from collapse to

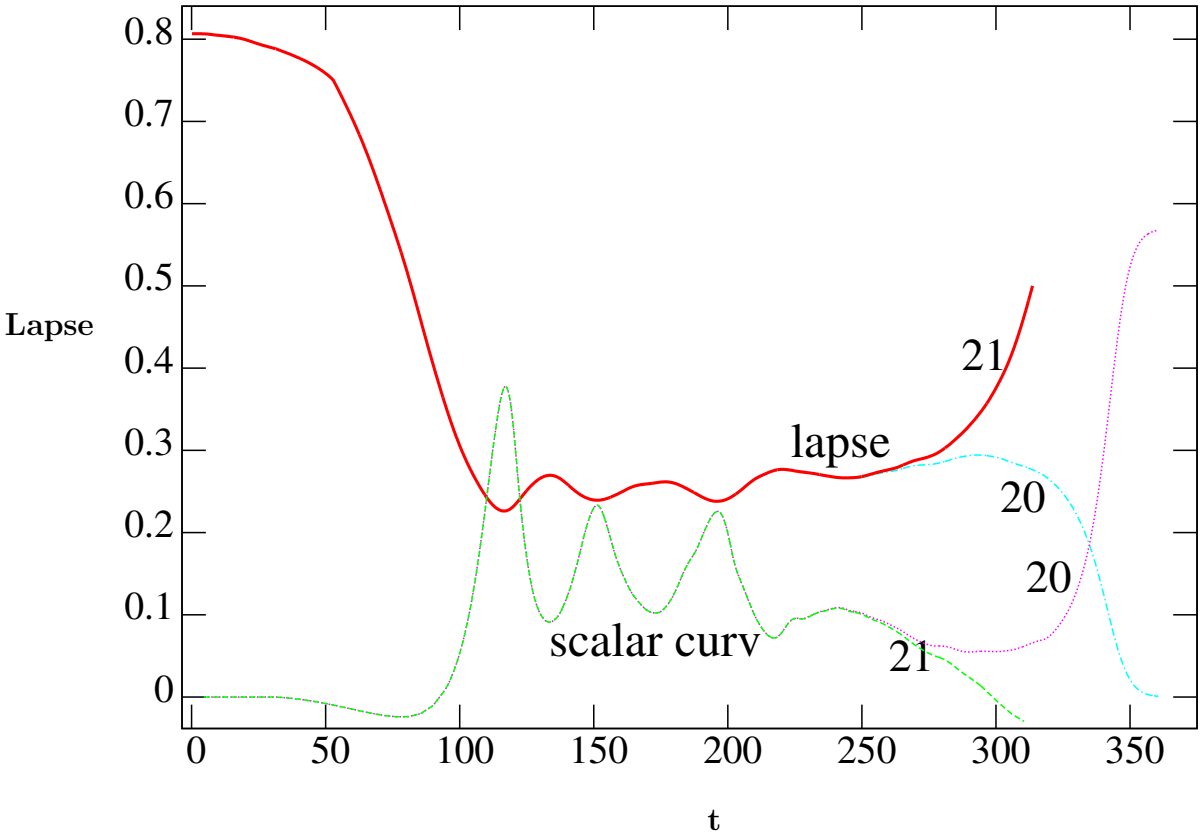


Figure 4.2: Comparing the lapse functions and the 4-d scalar curvatures for the cases of lines 20 and 21 in Fig. 4.1.

no collapse. In Fig. 4.1 we see that for these near critical configurations $\alpha$ oscillates at about 0.255 with a period of $\sim 40M_{\odot}$. As the lapse is given by the determinant of the 3 metric, this represents an oscillation of the 3 geometry.

For a more invariant measure, in Fig. 4.2 we plot as dotted and long dashed lines the 4-D scalar curvature $R$ at the collision center for two of the near critical solutions (lines 20 and 21 in Fig. 4.1; they are the last ones to move away from the exact critical solution at $t \sim 300M_{\odot}$). We see that $R$ oscillates with the same period as the determinant of the 3 metric (the lapse). As $\alpha$ collapses to zero, $R$ blows up and

in each such case we find an apparent horizon, indicating the formation of a black hole. Similar oscillatory behavior has been seen in other critical collapse studies [26, 27, 3, 2]. We note that at late time $R$ of the sub-critical case (line 21) tends to a small negative value as a static TOV star should.

We note that while in Fig. 4.1 a change in the $10^{th}$ significant digit of the total mass of the system can change the dynamics from that of sub-critical to supercritical, this does not imply that we have determined the critical point to the $10^{th}$ digit of accuracy. The exact value of the critical point is affected by the resolution of the numerical grid as well as the size of the computational domain. We have performed high resolution simulations with 76 grid points per $R$, (with computational domain covering $8.5R$), and large computational domain simulations covering $34R$ (with resolution 38 grid point per $R$). Convergence tests in both directions of resolution and size of the computational domain suggest that the total mass of the critical solution in the head-on collision case with the EOS given is at $1.58 \pm 0.05 M_{\odot}$, with the error bound representing the truncation errors.

In Fig. 4.1 we used dx=0.12 and a grid size 38.76. We confirm our results using different resolutions, dx=0.16 in Fig. 4.3 and 0.24 in Fig. 4.4. Domain size for Fig. 4.1,. 4.3 and 4.4 are the same. In Fig. 4.5 we use dx=0.12 as in Figs. 4.1 but with 4 times the domain size. We thus confirmed the convergence of our result in terms of both resolution and boundary size.

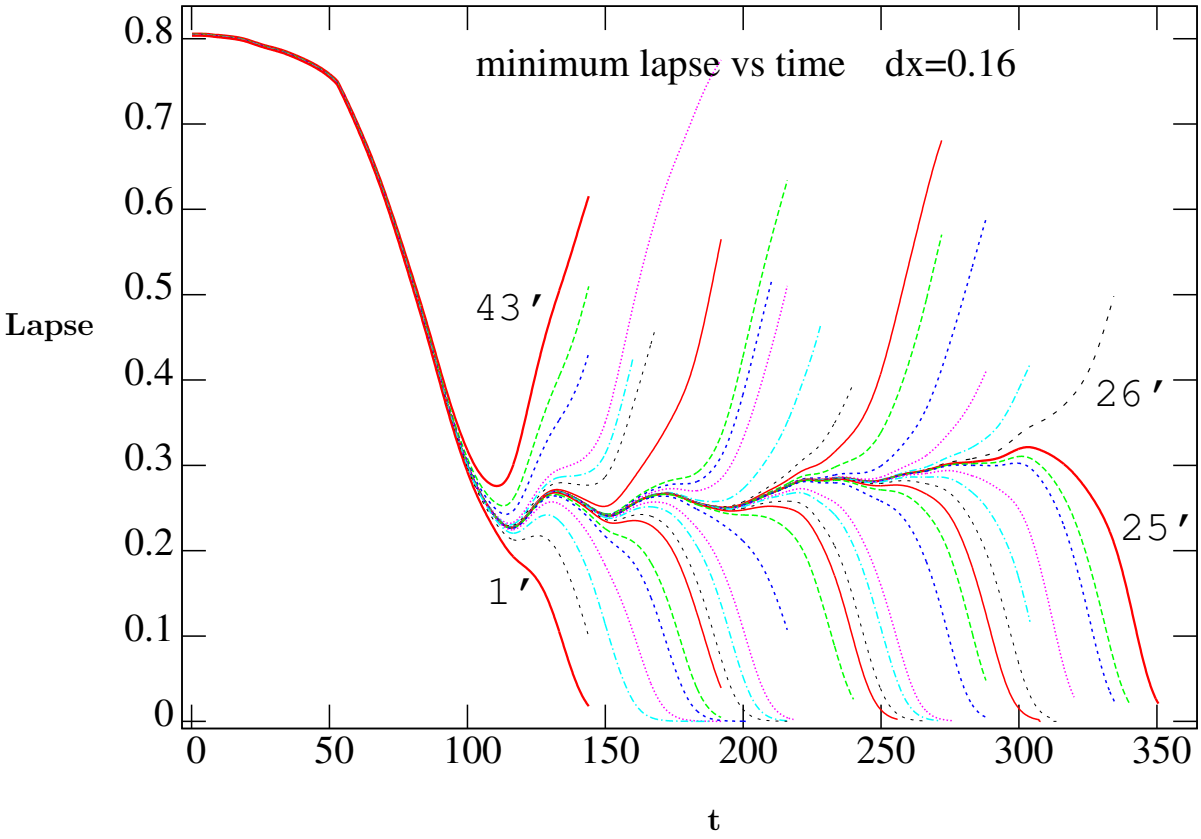


Figure 4.3: Lapse functions at center of collision vs. time for NSs with slightly different masses, dx=0.16.

## 4.4 Critical index

### 4.4.1 Definition

The critical index $\gamma$ is determined through the relation $T = \gamma \log(p - p_*)$, where $T$ is the length of the coordinate time (which is asymptotically Minkowski) that a near critical solution with a parameter value $p$ stays near the exact critical solution with $p_*$. [3, 4] In Sec. 3 above, $p$ is taken as the central density $\rho_c$ of the initial NSs. In Fig. 4.6, we plot $(\alpha - \alpha_*)/\alpha_*$ at the center of collision against the coordinate time,

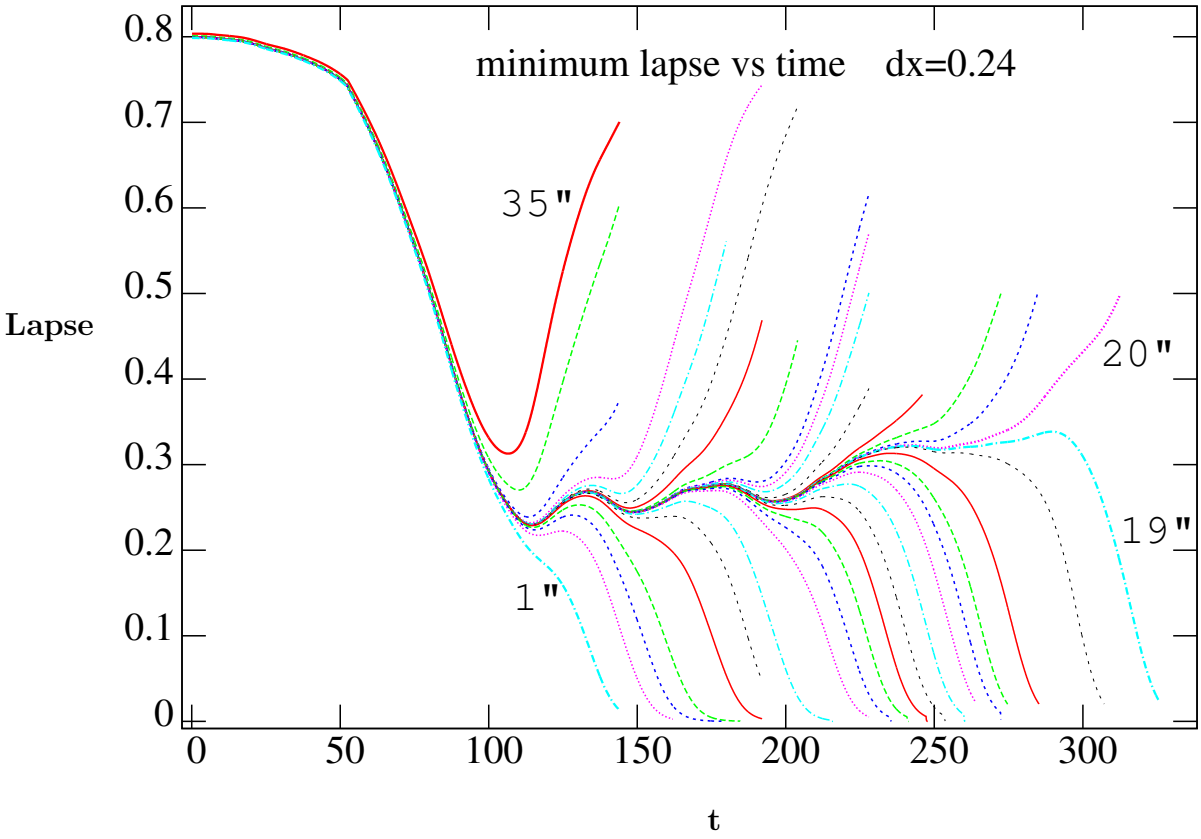


Figure 4.4: Lapse functions at center of collision vs. time for NSs with slightly different masses, dx=0.24.

where $\alpha_*$ is the lapse of the critical solution to the best we can determine. Only the last part of the evolution is shown. We see explicitly the growth of the unstable mode driving the near critical solution away from the critical solution. We defined the "departure time" $T_{0.05}$ as the coordinate time that a line in this figure reaches $\pm 0.05 = \pm 5\%$. Likewise we define $T_{0.1}$, $T_{0.15}$ and $T_{0.2}$. In Fig. 4.7, the departure times $T_{0.05}$ and $T_{0.2}$ are plotted against the log difference of $p$ (taken to be $\rho_c$ as in Fig. 4.1) between the near critical and the critical solutions. With this, $\gamma_{0.05}$ defined as $T_{0.05}/\log(p - p_*)$ is found to be 10.87, whereas $\gamma_{0.10}$, $\gamma_{0.15}$ and $\gamma_{0.2}$ are found to be

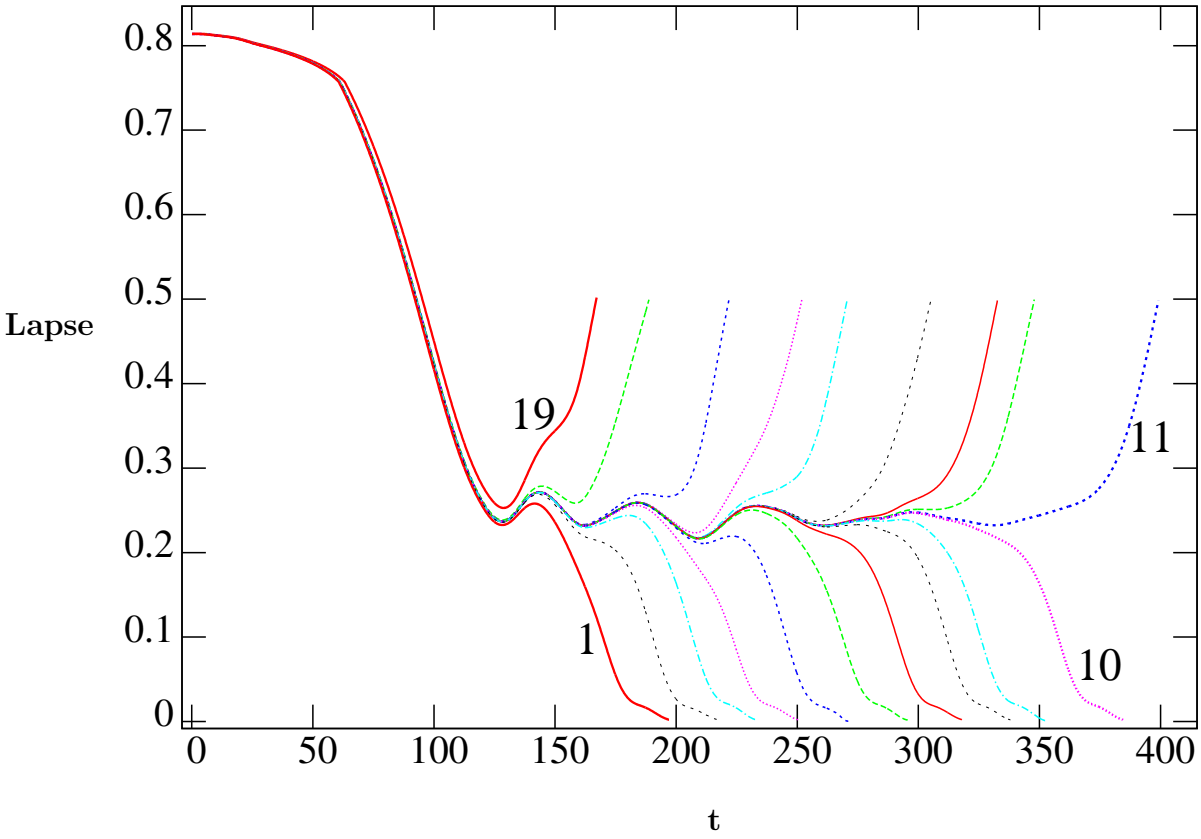


Figure 4.5: Lapse functions at center of collision vs. time for NSs with slightly different masses, dx=0.12, 4 times the grid size as figs. 4.1

$10.92, 10.93$ and $10.92$ respectively. We see that the value of the critical index does not depend sensitively on the definition of the departure point.

### 4.4.2 Convergence of the index

We see a basically 1st order convergence in Fig. 4.8, as expected. This shows the convergence of our code for the critical collapse situation. We note that near the critical point we cannot use the usual convergence test, since a tiny variation of the initial data may lead to a very different final state.

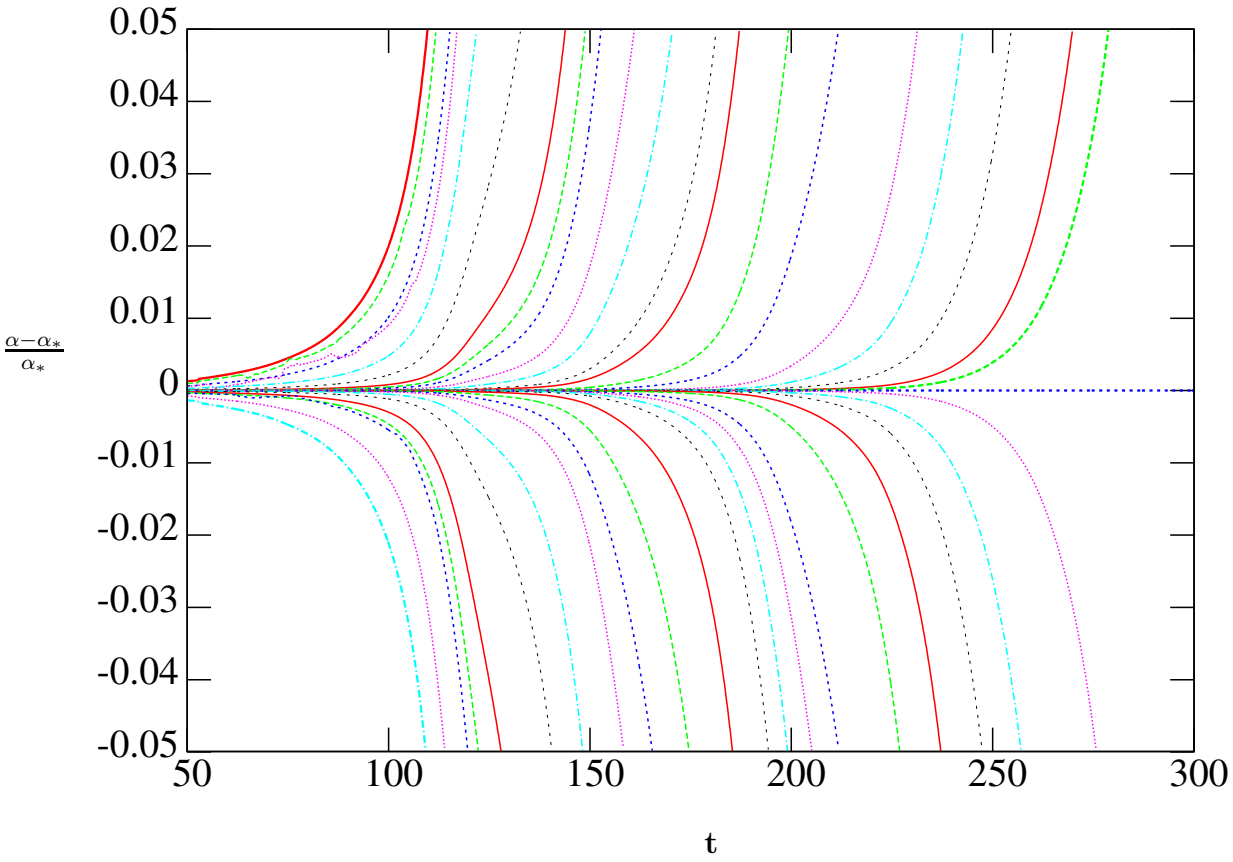


Figure 4.6: $(\alpha - \alpha_*)/\alpha_*$ vs. coordinate time.

## 4.5 Universality

### 4.5.1 Universality

The above study uses the total mass/central density of the initial NSs as the critical parameter $p$. Next we fix the central density $\rho_c$ of the initial NSs at $6.12820305495 \times 10^{-4} {M_\odot}^{-1}$. The initial coordinate separation between the center of the two NSs is fixed to be $D = 27.5 M_\odot$. The initial velocity $v$ is taken to be the parameter $p$. For each choice of $v$, the Hamiltonian and momentum constraint equations are solved.

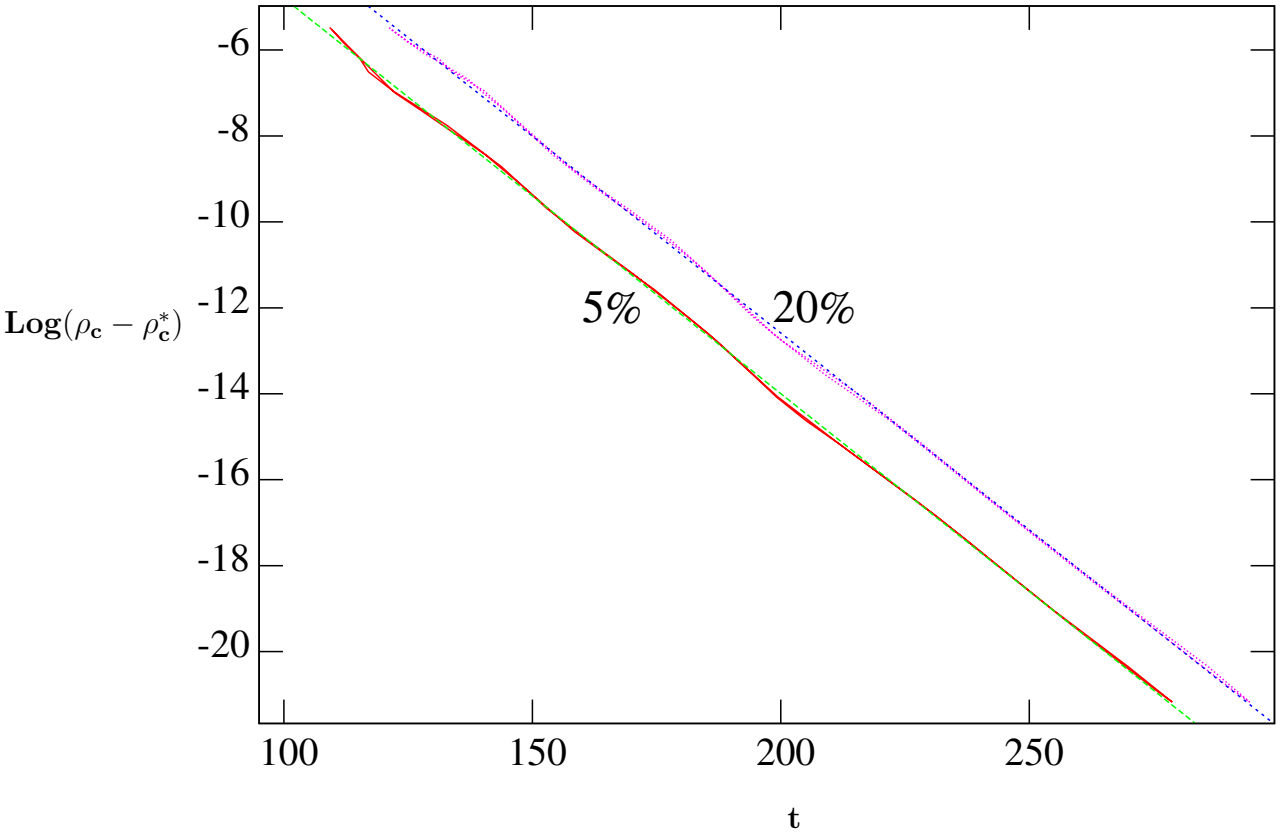


Figure 4.7: $Log(\rho_c - \rho_c^*)$ vs. the departure time determined with Fig. 4.6; the slope gives the critical index.

The results is shown Fig. 4.9. Convergence with respect to spatial resolutions and outer boundary location has been verified. We find the same critical phenomena. The critical index is extracted in the same manner and found to be $10.78 M_\odot$.

Other choices of parameter $p$ have also been studied, including:(i) $p = D$, while fixing $\rho_c$ and $v$, and (ii) $p = \rho_c$ while fixing $v$ and $D$. Note that the latter case is different from the case discussed in Secs. 3 and 4 above, where the initial velocity is determined by the free fall velocity up to the first PN correction. In all cases studied, we see the same critical phenomena with consistent values of the critical index $\gamma$.

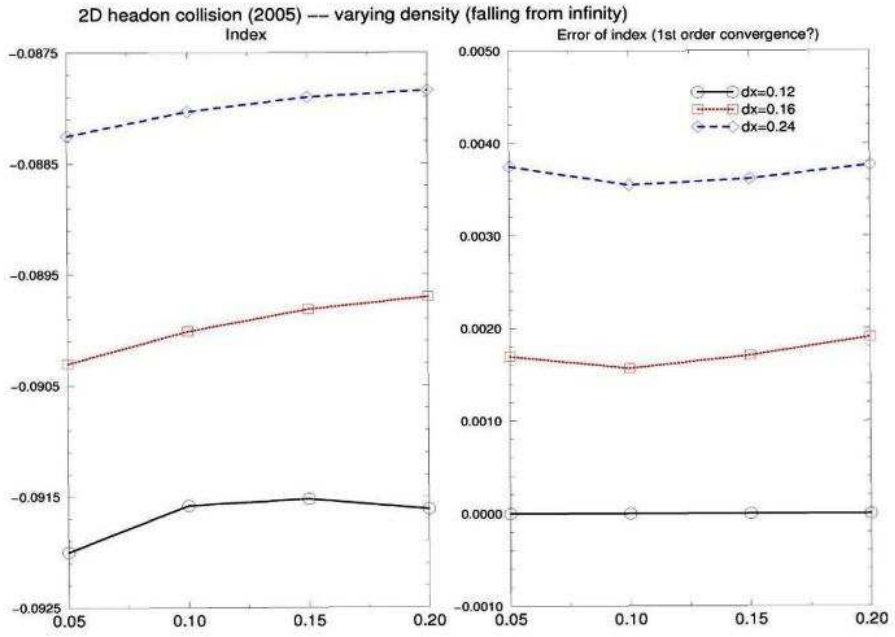


Figure 4.8: Left side: critical indices calculated for 3 resolutions with 4 different cutoff. Right side: errors relative to the highest resolution.

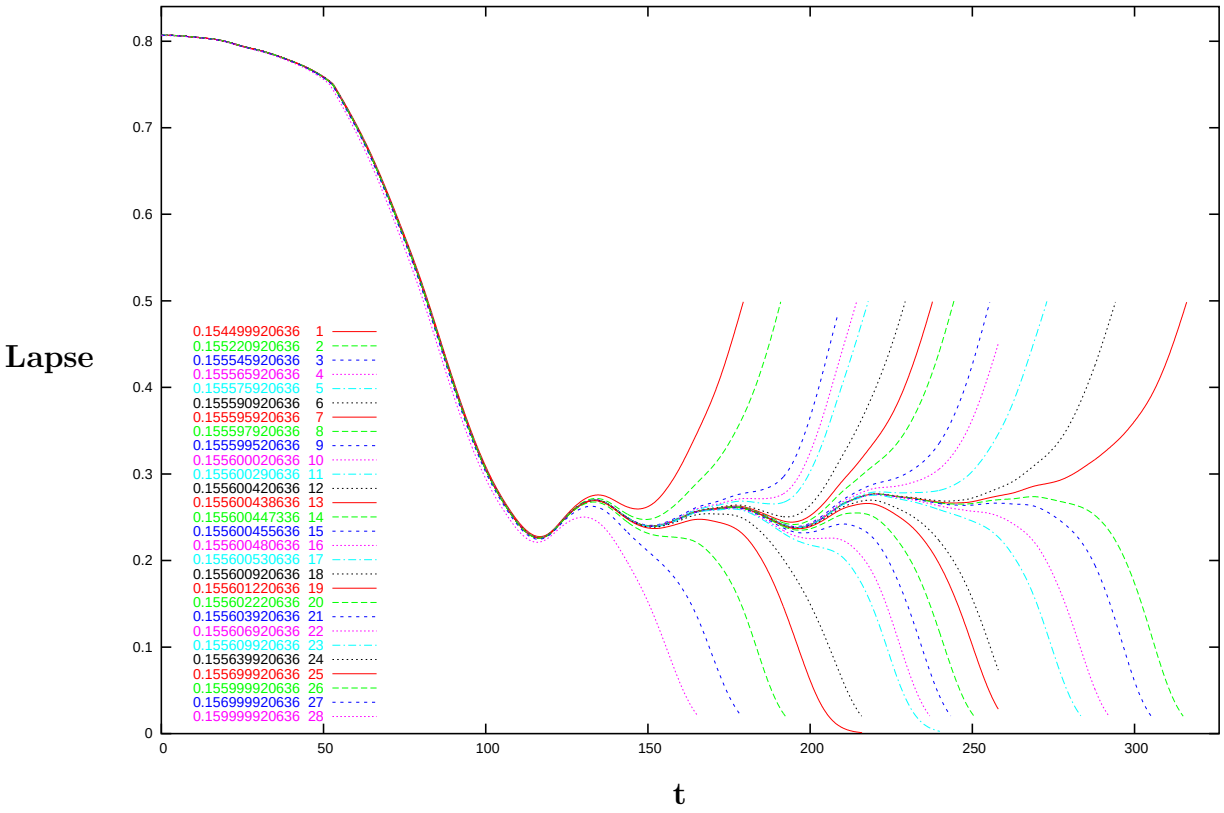


Figure 4.9: Lapses at the collision center for systems with the boosting velocity at the initial time.

Next we ask: Is critical collapse possible only through fine tuning the initial data? If true, we would not expect to see critical collapse phenomena in nature. We investigate the possibility of taking $p = \Gamma$, the adiabatic index, as slow changes of the EOS could occur in many astrophysical situations, e.g., accreting NSs and during cooling of proto-NSs generated in supernovae. We fix $D$, $\rho_c$, $v$ and vary $\Gamma$ away from 2. The evolution of the lapse at the center of collision is shown in Fig. 4.10. We see behavior similar to that of Fig. 4.1. The critical index $\gamma$ is found to be again $10.78 M_\odot$, consistent with the values found by fine tuning the initial configurations.

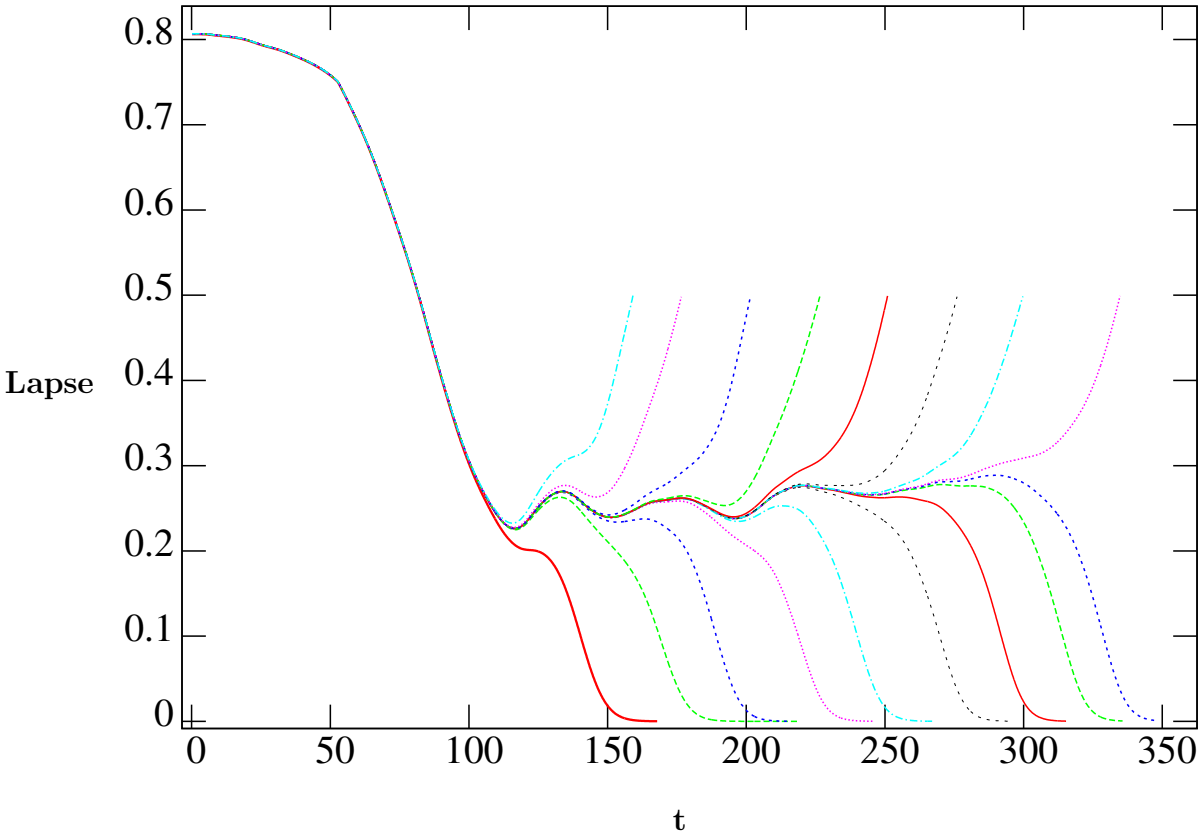


Figure 4.10: Lapses at the collision center for systems with the polytropic index $\Gamma$ varying between 1.9997 and 2.0001.

### 4.5.2 Possibility of being observed in nature

The system we studied is one step closer to reality in the sense that the EOS used is closer to that of a realistic astrophysics object, in two ways: (i) The stiff fluid EOS $P = K\rho$ used in previous studies by other research groups is special in that it is scale invariant, a central property for many systems of type II collapses (for review see [3]). The EOS we used $P = (\Gamma - 1)\rho\epsilon$ breaks scale invariance. (ii) Further, $P = K\rho$ is a one dimensional EOS, whereas $P = (\Gamma - 1)\rho\epsilon$ is two dimensional, as is generic for a

thermodynamic system (3 dimensional if chemical/nuclear reactions are included).

However, one would still not expect the critical collapse in our study to be observable in nature. First, an exact headon collision of two NSs is not likely to occur, although the assumption of axisymmetry is already one step more general than the assumption of spherical symmetry used in most existing critical studies. The second and more important reason is that one has to tune the initial parameter to high accuracy in order for the collapse to show critical behavior, e.g., when $p$ is chosen to be the central density $\rho$ of the NSs, we have to tune $(p - p_*)/p_*$ to smaller than $10^{-4}$. This is highly unlikely to occur in nature, given that there is no known astrophysics mechanism that would drive the density to this particular value.

What changes the situation is that we found that the same critical collapse could be triggered by a change of the polytropic index $\Gamma$ in the EOS [28]. In Fig. 4.10 we show the same oscillations of $log(g)$ for a range of $\Gamma$ near a critical value $\Gamma_*$. The critical index $\gamma$ is found to be again $\gamma = 10.78(\pm 0.06)M_\odot$.

This implies that for merged objects which may not be massive enough to collapse promptly, but will collapse after losing thermal support, we may see critical phenomena without fine tuning of initial data: The dominant cooling process, namely neutrino radiation, is on the timescale of seconds. The EOS will therefore be softening on this timescale, which is significantly longer than the time scale of growth ($\sim 0.05ms$) of the unstable mode of the IA. In losing thermal support, the merged object will gradually approach the threshold and evolves towards the IA, until the unstable mode kicks in causing a collapse to occurs in $\sim 0.05ms$. We note that this

will not be possible if the growth timescale of the unstable mode is longer than the timescale of the softening of the EOS. In that case, with the EOS quickly softening, the merged object will pass through the threshold region, and before the unstable mode has time to develop, the merged object will be well on the supercritical side and collapse without showing any critical behavior.

## 4.6 Phase space diagraph

### 4.6.1 Branches of critical solutions

In all previous studies for all choices of the parameters $p$, including $p$ equals to some size parameter of the system, rest mass of the system, ADM mass of the system, central density, field strength etc, there is a unique $p_*$, for which when $p > p_*$ a black hole is formed, and $p < p_*$ gives otherwise [5, 29, 2, 3, 4]. In our case, we found that for the phase space under investigation, for many choices of the parameter $p$, the value of $p_*$ is not unique. Namely, when $p < p_*$, the evolution leads to a neutron star, for $p_* < p < p_*^{'}$, the evolution leads to a black hole. However for $p > p_*^{'}$, the evolution leads to a neutron star again. We first observed this phenomena with the choice $p = v$, the initial speed of collision for the two stars starting at fixed distance $d$ with fixed initial central density $\rho_c$ (for our problem of head-on collision of two neutron star with a given EOS, the initial data has three parameters, namely, $v$, $d$, and $\rho_c$). In Fig. 4.11 we show the evolution of the lapse function for various initial speed $v$. Line 1 in this figure represents the one with the smallest $v$ ($= 0.129317340017$). We gradually

increase $v$ to 0.129514015227 represented by line 9 in the figure in 9 steps (hence 9 lines in the figure), the evolutions all lead to a neutron star. We see in Fig. 4.11 the lapse increases when the instable mode of the critical solution sets in, and an oscillating neutron star is formed (the later part of evolution not shown). However if we increase $v$ further to $v = 0.129514015270$, which is represented by line 10, a black hole is formed. The critical value of $v$ ($p_*$) is hence $0.129514015227 < p_* < 0.129514015270$. If we further increase $v$, we see the unstable mode sets in at earlier time, as we move further away from the transition surface between forming a neutron star and a black hole. At $v = 0.130837340017$, represented by line 19, a black hole is formed at time less than one oscillating of the lapse. All that are familiar.

What is interesting is that if we further increase $v$ to 0.172427340017, represented by line 1 of Fig. 4.12, again with the same $d$ and $\rho_c$. We see that a black hole is formed if we further increase it by 8 steps to $v = 0.172797483917$, represented by line 8 in Fig. 4.12. We see that in all 8 cases a black hole is formed, but the unstable mode sets in at a later and later time, indicating that $v$ is getting close to another critical value $p_*^{'}$, which is in between the $v$ of line 8 and the $v = 0.172797506017$ of line 9. From line 9 to 12 ($v = 0.173147340017$), a neutron star is formed at earlier and earlier time with increasing $v$.

### 4.6.2 Phase diagram of neutron star critical collapses

For the three dimensional initial phase space of neutron star collapses parameterized by $d$, $v$ and $\rho_c$ (respectively, the coordinate distance between the neutron stars on

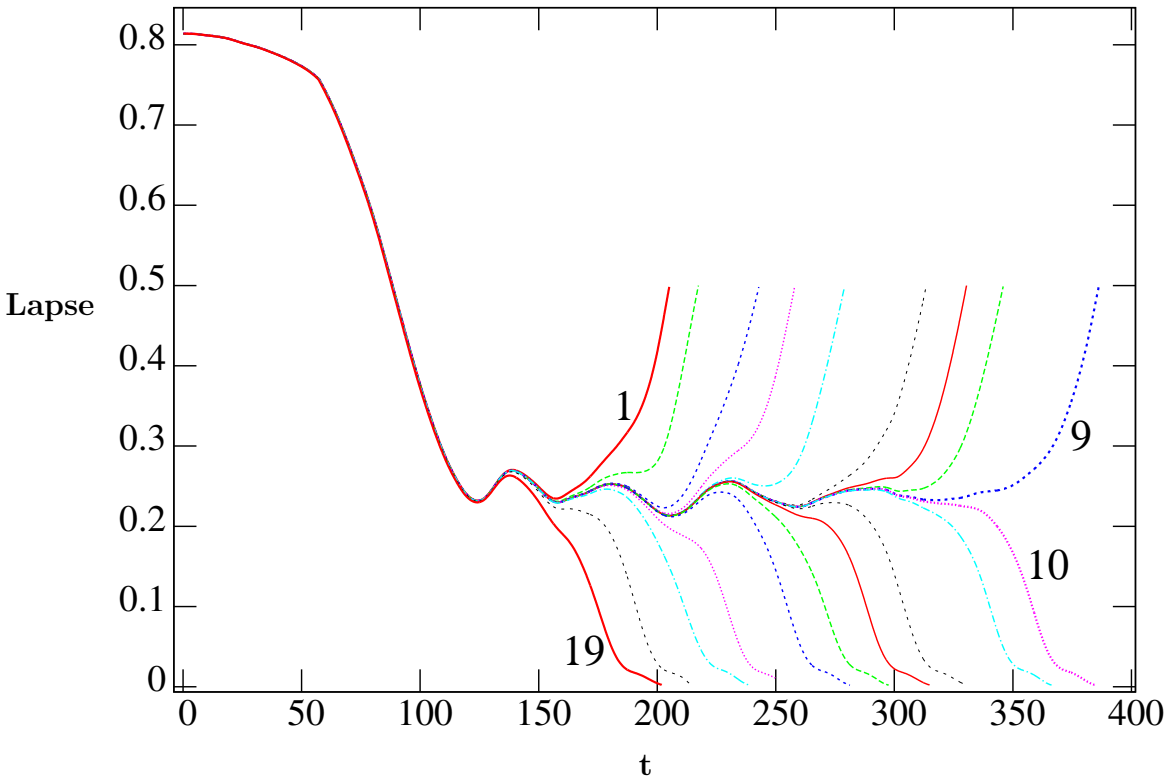


Figure 4.11: Lapse functions at center of collision vs. time for NSs with slightly different speeds.

collision course, the initial boosted speed and the central density), we fixed $d$ to be $13.60M_{\odot}$ to form a two dimensional phase space. Fig. 4.13 shows critical points on this two dimensional space. The horizontal axis is $v$, vertical axis is the central density $\rho_c$ (all in geometric units of G=c=1 with $M_{\odot}$=1 as in everywhere else in this thesis). For an initial configuration in the lower portion of the figure below the $\nu$-shaped line, a neutron star would be formed.

For example, for two neutron stars with central density 6.02098591836936e-4, and zero initial boost velocity, the evolution leads to a neutron star. When we increase

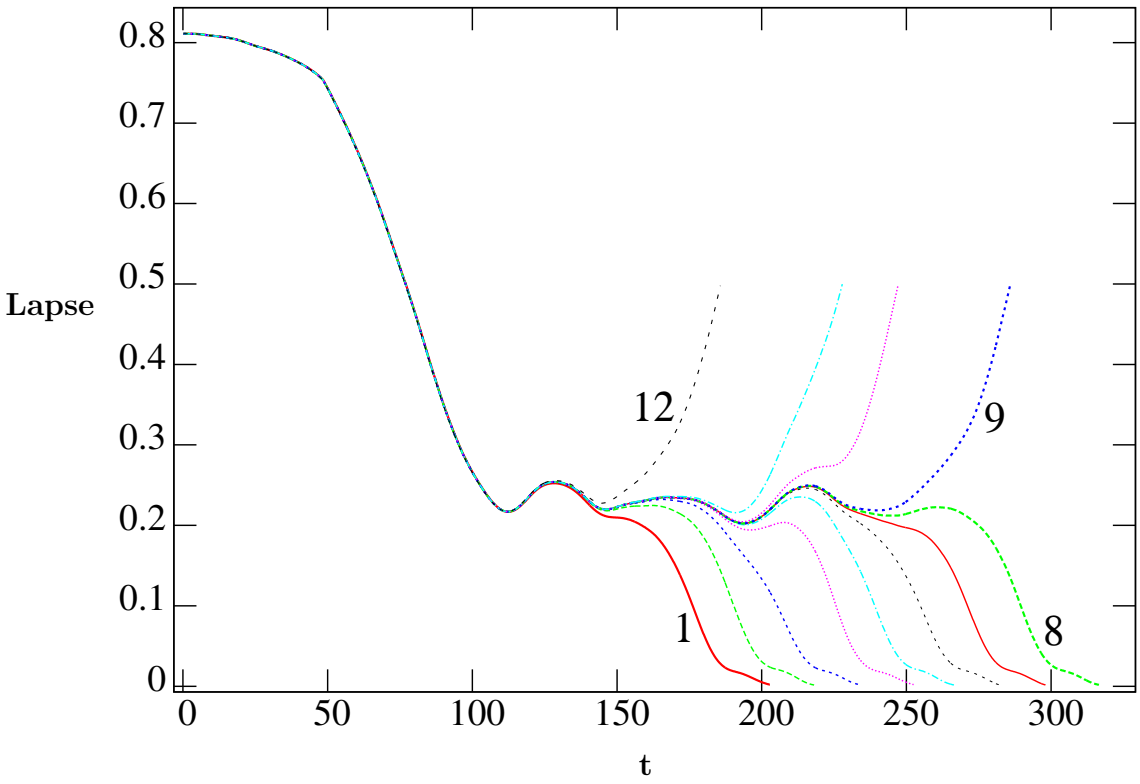


Figure 4.12: Lapse functions at center of collision varies in reversed direction as in Fig. 4.11.

the boost velocity to around 0.0791,we see the critical phenomena, as represented by the arrow in Fig. 4.11. The exact critical value is at $v = p_* \simeq 0.079167082107$. If we move further to the right in this figure, i.e., increase the velocity further, a black hole is formed. This is the central region of Fig. 4.13 labeled by "BH". If we further increase the velocity keeping $\rho_c$ fixed, at around $v \simeq 0.2541$ we encounter the 2nd branch of critical solution, which is the one shown in Fig. 4.12. Here the critical solution is at $v = \rho_c^{'} \simeq 0.2541728244276879$. If we further increase $v$ from this point on, a neutron star is formed.

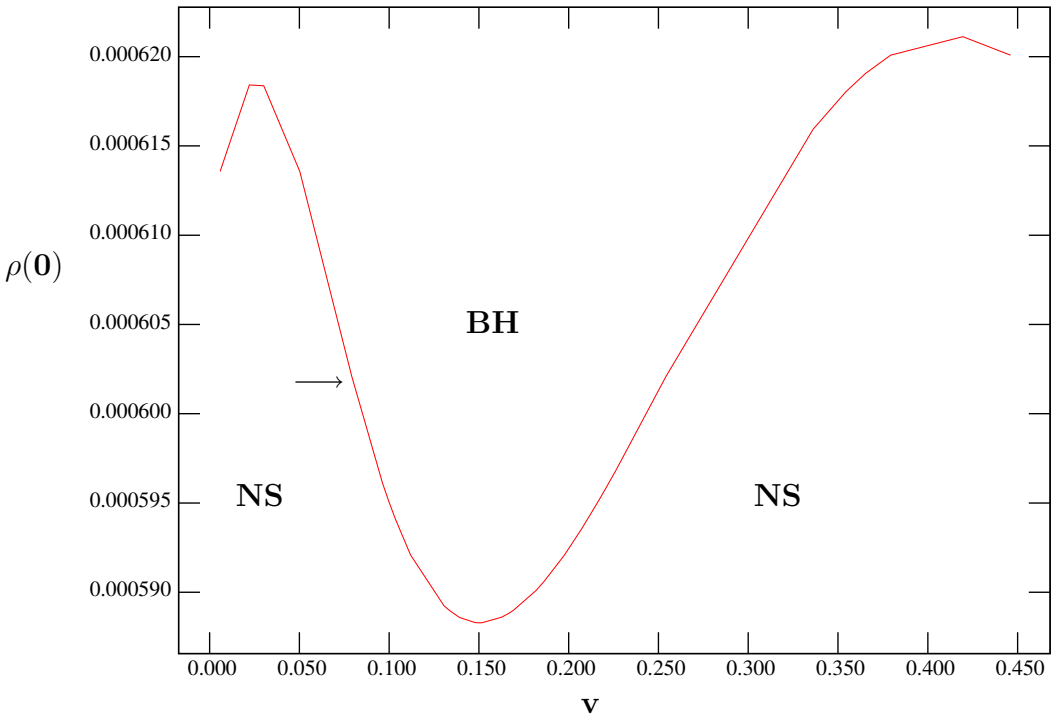


Figure 4.13: Central density vs. boosting velocity of critical solutions at initial time.

From Fig. 4.13, with $d$ fixed to be 13.60, we see that there exist a minimum value of $\rho_c \simeq 0.0005882895$, below which no black hole can be formed. This minimum value exists at boost velocity of $v \simeq 0.1503192$. There is also a maximum value of $\rho_c$ for forming neutron star. On the high velocity side, there is a global maximal value of $\rho_c \simeq 0.00062112$, appearing at $v \simeq 0.41950$. On the low velocity side, there is a local maximum at $\rho_c \simeq 0.00061842$, appearing at $v \simeq 0.022115$.

While one sees complicated structure of the phase diagram in $v$ vs. $\rho_c$, one may have concern that $v$ and $\rho_c$ are not geometrically invariant quantities. In Fig. 4.14, we plot the ADM mass of the system as the horizontal axis and the baryonic mass as the vertical axis. Again we see a $\nu-$*shaped* line. That the shape of lines representing the critical points are similar in Fig. 4.13 and Fig. 4.14 highlights the fact that $\rho_c$ is

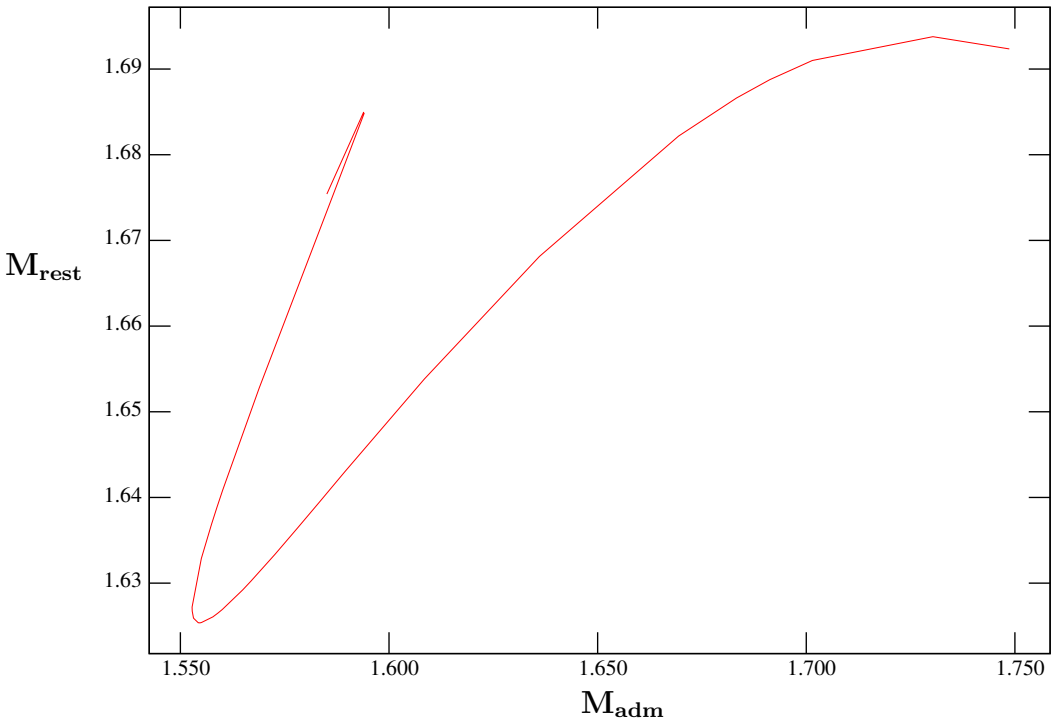


Figure 4.14: Total rest mass vs. total Adm mass of critical solutions at initial time.

closely related to the rest mass of the system, while the ADM mass which includes the kinetic energy of the system is significantly affected by the boost velocity. We see the same phenomena of different branches of critical solutions in Fig. 4.14, and the same complicated phase diagram.

This leads to a very intriguing question: Fig. 4.14 is in terms of the physical parameters of the system at the initial time. They are not directly related to the properties of the critical solution in the sense that the collision process emits gravitational wave, and hence the ADM mass of the initial configuration may not be directly related to the ADM mass of the critical solution itself as an isolated stationary compact object. It is obvious that the critical solution as a self-gravitating isolated compact object can be fully characterized by two parameters (two hairs in the sense of "hairs" of

black holes). The third piece of information in the 3 dimensional initial phase space $(d, v, \rho_c)$ must be "radiated" away. We can take the two parameters charactering the critical solution as an isolated compact object as the rest mass and the ADM mass of the solution. In view of Fig. 4.14, one may suspect that the rest mass and the ADM mass of the critical solution have an interesting relation.

However it is computationally difficult to extract the masses of the critical solution form the numerical evolution. In principle, one can carry the numerical evolution to a late time, using an outer boundary condition at the boundary of the computational domain that let gravitational wave as well as any matter ejection to pass through. One can then read out the rest mass and the ADM mass of the system consisting only of the isolated self-gravitating object. However, an out-going wave boundary condition has not been satisfactorily formulated for the Einstein theory despite many years of effort by our group and other research groups in the world. Beside the difficulties in formulating the out-going wave boundary condition, other difficulties in getting the masses of the critical solution include the need for long time evolution (which puts requirements on the resolution used that greatly increases the computational resource needed), and the use of a thinner artificial "atmosphere" in the numerical evolution [9] (which in turn increases the requirement on the stability of the primitive variable solver [30, 15]).

In Fig. 4.15 we show preliminary results of the relation between the rest mass and the ADM mass of the critical solution. These are the masses extracted at the 3rd extremum of the oscillation (e.g. around t $\sim$ 158 in Fig. 4.11). The horizontal

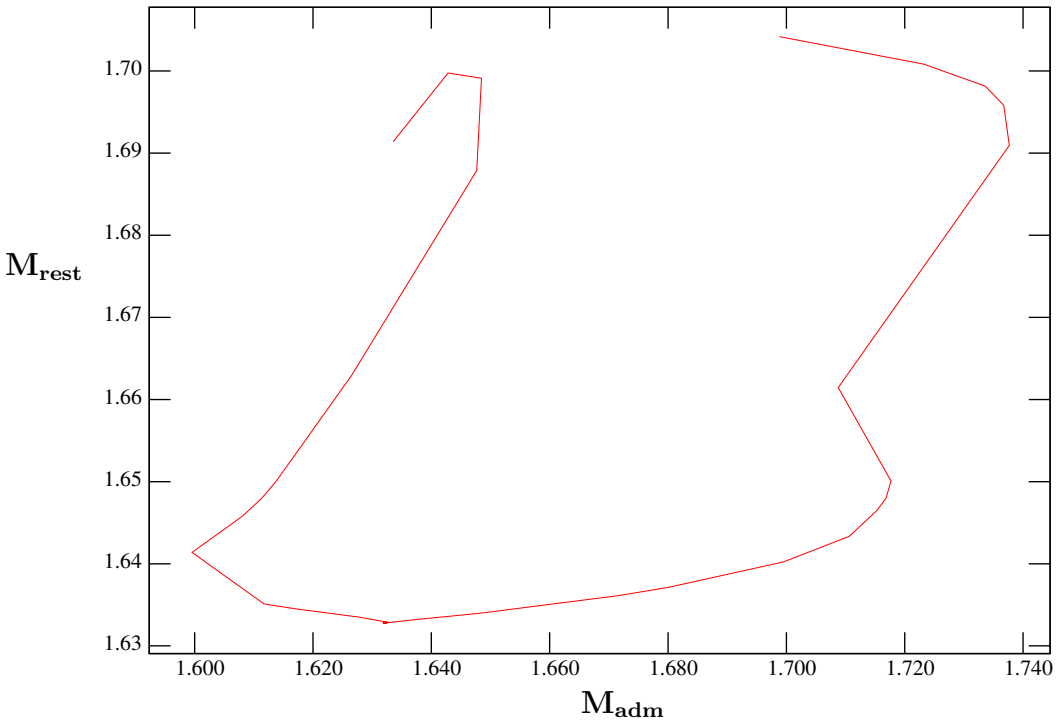


Figure 4.15: Total rest mass vs. total Adm mass of critical solutions at the 3rd extremum.

axis is the ADM mass, while the vertical axis is the rest mass. The simulations have been carried out at a resolution of dx=0.12, at 88 grid points per radius of the initial neutron star. Indeed we see an non-trivial relation between the rest mass and the ADM mass of the system, with many turning points. If these turning points are real, they may have relation to the number of unstable modes of the solutions. However further work would have to carried out to refine and confirm the result.

In Fig. 4.16, we plot the critical index of the critical solution (the vertical axis) vs. the rest mass (the horizontal axis) of the system. The critical index is a direct indication of the timescale of the unstable mode of the system (c.f. Sec. 4.4.1). Again we see different branches of critical solutions. Starting with the minimum rest mass of 1.625 that a critical solution can be formed, the critical index $\gamma$ is 10.35. As the rest

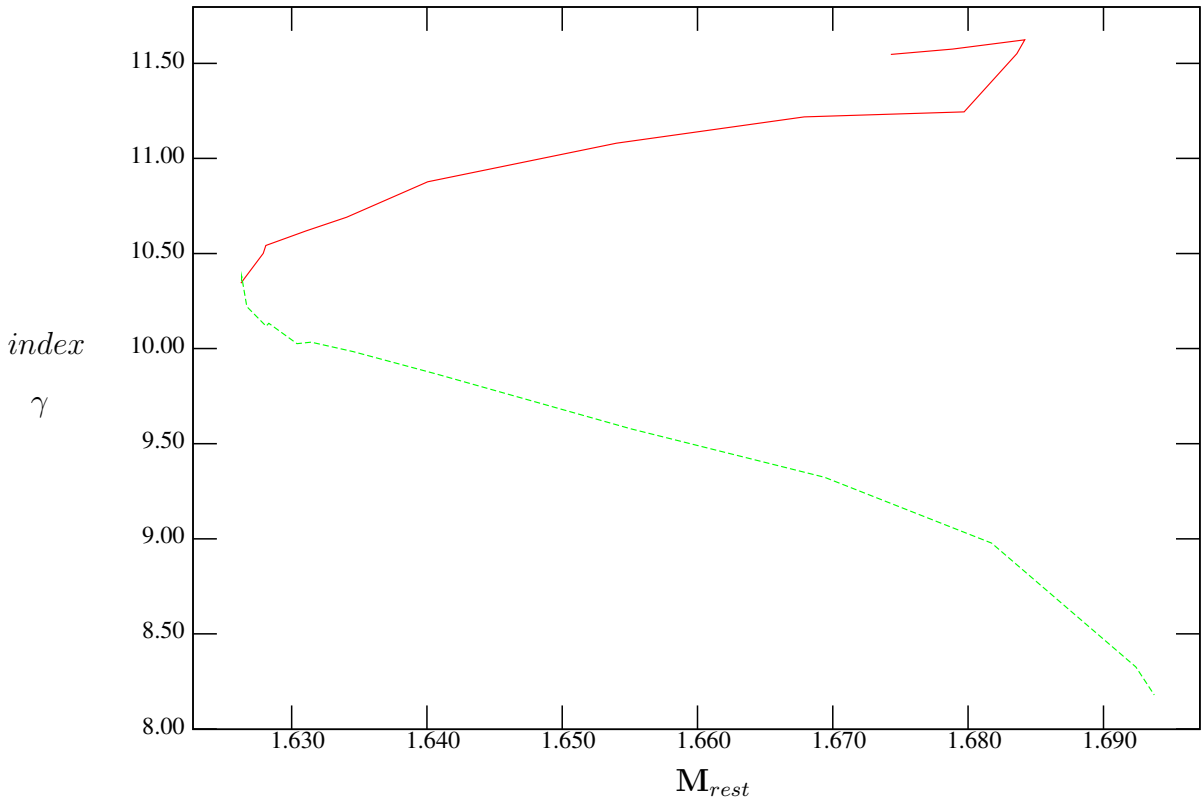


Figure 4.16: The variation of critical index respect to the total rest mass of the system.

mass increases, one branch has $\gamma$ decreasing while another branch has $\gamma$ increasing. However at large rest mass of around 1.682, the upper branch has another turning point connecting to a third branch. Again further investigation must be done to confirm this behavior.

In conclusion, the critical phenomena of gravitational collapse of compact object is rich and interesting.

# Chapter 5

# Conclusion and discussions

We showed that critical gravitational collapse can occur with an equation of state(EOS) commonly used in describing neutron star matter, and with a non-spherical initial configuration. We further showed that critical collapses can occur due to an adiabatic change of the EOS. This coupling with the fact that the dynamical time scale of evolution towards to intermediate attractor (IA) (of order milliseconds) when the star is near the critical surface, and the dynamical time scale of the unstable mode of the IA (also of order milliseconds), are both much shorter than the dissipation time scale of the system (of order seconds) suggests that we might be able to observe the critical collapse phenomena in newly formed neutron matter compact objects, like proto-neutron stars formed in supernova and hyper massive neutron stars in neutron star binary coalescences.

However, the thesis has not answered the questions of whether "critical collapses can be observed in nature" in full. To answer this question, further research in the

following two directions must be carried out: (1) How "wide" is the "window of critical collapse" in binary neutron star coalescence (or supernova)? And (2), what are the characteristics of gravitational wave signals and neutrino radiation signals that we can observe from a critical collapse?

We have obtained various preliminary results for both of these questions, which are not included in Chapter 4 of this thesis. These include: (1) Critical collapses with angular momentum. We constructed head-on collisions of the neutron star with spins. The merged object has non-trivial angular momentum. We observed again critical phenomena. While the IA for the case without angular momentum is a limit cycle, when angular momentum is added, instead of a limit cycle, the trajectory of a near critical solution would spiral into a fixed point, with an increasing "rate" of inspiral for larger angular momentum. This is the first step towards the study of critical phenomena in a binary coalescence which always comes with angular momentum. (2) Through comparing the critical solutions with angular momenta obtained in the axisymmetric study with the full 3D simulations of binary coalescence of neutron stars with the same EOS carried out by other members of our research group, we obtained evidence that critical collapses can occur in the full 3D situation without axisymmetry. We see critical collapses at the boundary line between the prompt and delayed collapses (Zhang et al [9]). (3) On the question of observable signals from critical collapses, we obtained preliminary results indicating that in the case of zero angular momentum the unstable mode of the critical solution is spherical. A collapse through a spherical mode emits no gravitational wave. This means that a

non-spherical object near the critical surface will radiate all its asymmetry away while evolving towards the critical solution. And the final collapse of the compact object would be "silent" in term of gravitational radiation. We can observe only neutrino signals of the final collapse without an accompanying gravitational wave signal. If confirmed, this would suggest that there would be a class of gravitational collapses which are gravitationally "silent". Would the unstable mode of a critical solution with a significant angular momentum also be spherical? This is the next question we plan on investigating.

We have not fully confirmed and included these results in Chapter 4 of the thesis. We note that each simulation described in this thesis involves solving the Einstein equation coupled with the general relativistic hydrodynamic equations with thousand of terms, involving hundreds of variables and they must be updated on millions of grid points for tens of thousands of time steps. Each simulation requires hundreds of hours even on the massively parallel supercomputers of the national supercomputing centers. To confirm one critical solution with, say, a given rest mass and a gravitational mass, and find its critical index, tens if not hundreds of simulations must be carried out. The construction of the numerical code, its validation with many convergence tests (Chapter 3 gives just the most significant ones), together with the results presented in Chapter 4, have taken many years of intense research effort.

Since the publication of our paper [28], other researchers have followed up in this direction [31, 32].

# Bibliography


[1] M. W. Choputik. Universality and scaling in gravitational collapse of a massless scalar field. *phys. Rev. Lett*, 70:9, 1993.

[2] A. Z. Wang. Critical phenomena in gravitational collapse: The studies so far. *Braz.J. Phys.*, 31(2):188–197, 2001. gr-qc/0104073.

[3] C. Gundlach. Critical phenomena in gravitational collapse. *Physics Reports*, 376:339, 2003. gr-qc/0210101.

[4] C. Gundlach. Critical phenomena in gravitational collapse. arXiv:0711.4620.

[5] Chris M. Chambers Patrick R. Brady and Sergio M. C. V. Goncalves. Phases of massive scalar field collapse. *Phys. Rev. D*, 56:R6057, 1997. gr-qc/9709014.

[6] S. H. Hawley and M. W. Choptuik. Boson stars driven to the brink of black hole formation. *Phys. Rev. D*, 62:104024, 2000.

[7] Ignacio Olabarrieta and Matthew W. Choptuik. Critical phenomena at the threshold of black hole formation for collisionless matter in spherical symmetry. *Phys. Rev. D*, 65:024007, 2002.

[8] Masaru Shibata, Keisuke Taniguchi, and Koji Uryu. Merger of binary neutron stars with realistic equations of state in full general relativity. *Phys. Rev.*, D 71:084021, 2005.

[9] K.-S. Cheng, W.-M. Suen, J. Tao, M.-B. Wan, R. Wolfmeyer, and H.-M. Zhang. How much angular momentum is needed to support against a prompt collapse in neutron star mergers? *Phys. Rev. Lett.* Submited.

[10] C. W. Misner, K. S. Thorne, and J. A. Wheeler. *Gravitation*. W. H. Freeman, San Francisco, 1973.

[11] Eric Gourgoulhon. 3+1 formalism and bases of numerical relativity.

[12] T. W. Baumgarte and S. L. Shapiro. On the numerical integration of Einstein's field equations. *Phys. Rev. D*, 59:024007, 1999. gr-qc/9810065.

[13] M. Alcubierre, B. Brügmann, T. Dramlitsch, J.A. Font, P. Papadopoulos, E. Seidel, N. Stergioulas, W.-M. Suen, and R. Takahashi. Towards a stable numerical evolution of strongly gravitating systems: The conformal treatments. *Phys. Rev. D*, 62:044034, 2000. gr-qc/0003071.

[14] M. Miller, P. Gressman, and W. M. Suen. Towards a realistic neutron star binary inspiral: Initial data and multiple orbit evolution in full general relativity. *Phys. Rev. D*, 69:064026, 2004.

[15] J. A. Font, M. Miller, W. M. Suen, and M. Tobias. Three dimensional numerical general relativistic hydrodynamics i: Formulations, methods, and code tests. *Phys. Rev. D*, 61:044011, 2000. gr-qc/9811015.

[16] Miguel Alcubierre, Bernd Brügmann, Peter Diener, Michael Koppitz, Denis Pollney, Edward Seidel, and Ryoji Takahashi. Gauge conditions for long-term numerical black hole evolutions without excision. 2002. gr-qc/0206072.

[17] C. Evans. An approach for calculating axisymmetric gravitational collapse. In J. Centrella, editor, *Dynamical Spacetimes and Numerical Relativity*, pages 3–39. Cambridge University Press, Cambridge, England, 1986.

[18] D. Bernstein, D. Hobill, E. Seidel, L. Smarr, and J. Towns. Numerically generated axisymmetric black hole spacetimes: Numerical methods and code tests. *Phys. Rev. D*, 50(8):5000–5024, 1994.

[19] M. Alcubierre, S. Brandt, B. Brügmann, D. Holz, E. Seidel, R. Takahashi, and J. Thornburg. Symmetry without symmetry: Numerical simulation of axisymmetric systems using cartesian grids. *Int. J. Mod. Phys. D*, 10:273–289, 2001. gr-qc/9908012.

[20] The source and documentation of the released code can be downloaded at http://wugrav.wustl.edu/Codes/GR3D. For credit of the code development, see the document http://wugrav.wustl.edu/Codes/GR3D/nasa_ms2.ps.

[21] M. Miller, W.-M. Suen, and M. Tobias. Shapiro conjecture: Prompt or delayed collapse in the head-on collision of neutron stars. *Phys. Rev. D. Rapid Comm.*, 63:121501(R), 2001.

[22] R. J. Leveque. *Numerical Methods for Conservation Laws*. Birkhauser Verlag, Basel, 1992.

[23] F. Banyuls, J. A. Font, J. M. Ibánez, J. M. Martí, and J. A. Miralles. Numerical 3+1 general-relativistic hydrodynamics: A local characteristic approach. *ApJ*, 476:221, 1997.

[24] David W. Neilsen and Matthew W. Choptuik. Critical phenomena in perfect fluids. *Classical Quantum Gravity*, 17:761, 2000. gr-qc/9812053.

[25] Edwin Evans, A. Gopakumar, Philip Gressman, Sai Iyer, Mark Miller, Wai-Mo Suen, and Hui-Min Zhang. Head-on/near head-on collisions of neutron stars with a realistic eos. *Phys. Rev. D*, 67:104001, 2003.

[26] M. W. Choptuik, S. L. Liebling E. W. Hirschmann, and F. Pretorius. Critical collapse of the massless scalar field in axisymmetry. *Phys. Rev. D*, 68:044007, 2003.

[27] A. M. Abrahams and Charles R. Evans. Universality in axisymmetric vacuum collapse. *Phys. Rev. D*, 49:3998, 1994.

[28] Ke-Jian Jin and Wai-Mo Suen. Critical phenomena in head-on collisions of neutron stars. *Phys. Rev. Lett.*, 98:131101, 2007. gr-qc/0603094.

[29] M. W. Choptuik. Critical behavior in gravitational collapse of a yang-mills field. *Phys. Rev. Lett.*, 77:424, 1996.

[30] J. M. Martí and E. Müller. *J. Comput. Phys.*, 123:1, 1996.

[31] Thorsten Kellerman, Luciano Rezzolla, and David Radice. Critical phenomena in neutron stars ii: Head-on collisions. gr-qc/1007.2792.

[32] David Radice, Luciano Rezzolla, and Thorsten Kellerman. Critical phenomena in neutron stars i: Linearly unstable nonrotating models. gr-qc/1007.2809.